

X-Ray Reflection Signatures of Supermassive Black Hole Binaries

JULIE MALEWICZ ¹, DAVID R. BALLANTYNE ¹, TAMARA BOGDANOVIĆ ¹, LAURA BRENNEMAN ², AND
THOMAS DAUSER ³

¹Center for Relativistic Astrophysics, School of Physics, Georgia Institute of Technology, 837 State Street NW, Atlanta, GA 30332-0430, USA

²Center for Astrophysics, Harvard-Smithsonian, 60 Garden Street, Cambridge, MA 02138, USA

³Dr. Karl Remeis-Observatory & ECAP, FAU Erlangen-Nürnberg, Sternwartstr. 7, 96049 Bamberg, Germany

ABSTRACT

We investigate the presence of supermassive black hole (SMBH) binary signatures and the feasibility of identifying them through X-ray reflection spectra. The X-ray emitting region is modeled as a set of two mini-disks bound to the individual SMBHs separated by $100 GM/c^2$ and the spectra calculated as a function of the mass, mass ratio, and total accretion rate of the binary. The X-ray reflection features are strongly influenced by the accretion-inversion phenomenon expected in SMBH binaries, which results in a wide range of ionization conditions in the two mini-disks. These are imprinted in the resulting composite spectra and the double-peaked and time-variable relativistic Fe K α line profiles. To test whether these features can be used as evidence for the presence of an SMBH binary, we fit mock 100 ks observations with a single AGN model. For a $10^9 M_\odot$ binary targeted by Pulsar Timing Arrays (PTAs), at $z = 0.1$ the single AGN model clearly fails to fit the data, while at $z = 1$ the fit is acceptable but unable to converge on the SMBH spin. For a $10^6 M_\odot$ binary, a progenitor of a *Laser Interferometer Space Antenna (LISA)* source, spectral fitting is only possible at $z = 0.1$, with the outcomes similar to the PTA binary at $z = 1$. We also find that PTA binaries can be expected to show a distinct X-ray spectral variability in multi-epoch observations, whereas for *LISA* precursors, orbital averaging results in the loss of spectral variability signatures.

1. INTRODUCTION

Supermassive black hole (SMBH) binaries are expected to be the natural byproducts of standard hierarchical galaxy formation (e.g., M. C. Begelman et al. 1980; T. Di Matteo et al. 2005; P. F. Hopkins et al. 2008). A bound binary will form after a galaxy merger when the two SMBHs reach a separation $\lesssim 1$ pc, after which the orbit slowly tightens through three-body interactions with nearby stars and local gas flows (e.g., F. Antonini et al. 2015). Finally, at separations of $\sim 10^{-3}$ pc, the emission of gravitational waves (GWs) begins to dominate the orbital evolution (e.g., P. C. Peters & J. Mathews 1963; A. Mangiagli et al. 2022), driving the binary towards merger. Detecting electromagnetic (EM) signatures of SMBH binaries during their orbital decay is of particular interest in the era of multimessenger astronomy, as they will provide crucial information and context for interpreting GW signatures from SMBH mergers (e.g., T. Bogdanović et al. 2022). Indeed, the recent detection of a stochastic GW background by millisecond

Pulsar Timing Arrays (PTAs; G. Agazie et al. 2023a; J. Antoniadis et al. 2023; D. J. Reardon et al. 2023; H. Xu et al. 2023) could be explained by numerous SMBH binaries locked in tight, sub-parsec orbits (e.g., G. Agazie et al. 2023b). Searches for the EM signatures of this population of SMBH binaries is crucial to understanding this background. The EM identification of SMBH binaries with sub-parsec separations must rely on indirect methods, as they cannot be spatially resolved using imaging with current instruments.

Galaxy mergers not only produce SMBH binaries, but also drive a significant inflow of gas to the central regions of the merger remnant (e.g., J. E. Barnes & L. E. Hernquist 1991; T. Di Matteo et al. 2005; P. F. Hopkins et al. 2005; S. Kazantzidis et al. 2005). This provides a favorable environment for the two SMBHs to accrete efficiently and shine as active galactic nuclei (AGNs) during their evolution (e.g., M. Volonteri et al. 2003; A. Sesana et al. 2012; A. De Rosa et al. 2019). AGN activity often produces emission lines from ionized gas bound to the SMBH; therefore, searches for changes or unusual offsets in these emission line profiles may be an avenue to find evidence of a SMBH binary (e.g., T. Bogdanović

et al. 2009; M. Eracleous et al. 2012; J. C. Runnoe et al. 2015). While on the order of one hundred SMBH binary candidates have been identified using the profiles of broad optical emission lines, uncertainties in the dynamics of broad-line region clouds, and the challenges of separating the signatures of a potential binary from a recoiling single AGN, make the interpretation of the results ambiguous (e.g., B. Husemann et al. 2020).

AGNs also often exhibit a fluorescent Fe $K\alpha$ emission from the inner accretion disk in their X-ray spectra (e.g., Y. Tanaka et al. 1995; L. W. Brenneman & C. S. Reynolds 2006; C. S. Reynolds 2013). This broad line originates from gas tightly orbiting the SMBH, sculpting its profile through relativistic effects (e.g., A. C. Fabian et al. 1989). The Fe $K\alpha$ line is one part of an overall reflection spectrum emitted by the accretion disk due to its irradiation by a central, hot corona (e.g., J. García & T. R. Kallman 2010; T. Dauser et al. 2014; D. R. Ballantyne 2017). Recent simulations of SMBH binaries show that each SMBH will be accreting from a ‘mini-disk’ that is fed from a larger circumbinary disk (e.g., B. D. Farris et al. 2014; D. B. Bowen et al. 2017; Y. Tang et al. 2018; M. J. Avara et al. 2024). If the mini-disks produce X-ray emitting coronae similar to those of single AGNs, then each accretion disk of the binary will produce its own reflection spectrum, including a relativistically broadened Fe $K\alpha$ line. The composite reflection spectrum may therefore contain signatures of the binary that could be identified with a sufficiently high-quality X-ray observation. Moreover, since the shape of the Fe $K\alpha$ line contains information on the spin of the central SMBH (e.g., C. S. Reynolds & A. C. Fabian 2008), fundamental properties of both SMBHs could, in principle, be accessible through fitting the combined Fe $K\alpha$ line.

Previous discussions of the X-ray spectra in SMBH binaries have either focused on the modeling of the Fe $K\alpha$ line in isolation, without accounting for the different ionization properties expected from mini-disks in unequal mass binaries (Q. Yu & Y. Lu 2001; L. Č. Popović 2012; P. Jovanović et al. 2014, 2020), or treated the emission as thermal in origin, without the presence of the full reflection spectrum (e.g., B. D. Farris et al. 2015; S. d’Ascoli et al. 2018). Here, we study the composite, relativistic, ionized X-ray reflection spectra, from roughly 0.1 to 100 keV, expected from two gravitationally bound SMBH binaries at a separation of 100 gravitational radii, taking into account the expected size of the mini-disks. We show how the composite spectra change as a function of the accretion rate onto the binary and the mass ratio of the two SMBHs. Finally, we evaluate the prospects for detection of any binary signatures by considering

mock observations from the next-generation X-ray missions currently in development.

In the next section, we lay out the details of our methods to model an accreting SMBH binary and compute its composite X-ray spectrum. Section 3 presents the resulting composite spectra for various combinations of mass ratio and total accretion rate onto the binary. Section 4 describes the simulated observations of a fiducial SMBH binary by 4 well-studied X-ray telescope concepts (*NewAthena*, *AXIS*, *HEX-P* and *STROBE-X*), as well as a preliminary time variability study of a promising configuration with *NewAthena*. A discussion of the implications and limitations of our results is found in Sect. 5, and overall conclusions are presented in Sect. 6.

2. METHODS

2.1. Composition of Binary System

We model SMBH binary systems composed of two near-maximally spinning (i.e., spin parameter $a = 0.99$) SMBHs with mass ratio $q = m_2/m_1$ where $0.1 \leq q \leq 0.9$, in a circular orbit separated by a distance of $s = 100 r_g$ ($r_g = GM/c^2$ is the gravitational radius for a binary with total mass $M = m_1 + m_2$). The total mass of the binary is set to either $10^9 M_\odot$ or $10^6 M_\odot$. The $M = 10^9 M_\odot$ binaries at $s = 100 r_g$ emit GWs within the PTA band (e.g., A. Sesana et al. 2012), while $M = 10^6 M_\odot$ binaries at this separation should enter the *LISA* sensitivity band by the time they merge. Following P. C. Peters (1964), the characteristic orbital and GW merger time scale for such binaries is

$$t_{\text{orb}} = 0.36 \text{ days} \left(\frac{M}{10^6 M_\odot} \right) \left(\frac{s}{100 r_g} \right)^{3/2}, \quad (1)$$

and

$$t_{\text{gw}} = 0.31 \text{ yr} \frac{(1+q)^2}{q} \left(\frac{M}{10^6 M_\odot} \right) \left(\frac{s}{100 r_g} \right)^4, \quad (2)$$

The difference in those two time scales for the SMBH binaries at this characteristic separation allows us to consider s as time-independent in our calculations. In what follows, we refer to the $10^9 M_\odot$ binaries as ‘PTA’ binaries and the $10^6 M_\odot$ binaries as ‘*LISA*’ binaries.

Each SMBH in the binary is accreting through a mini-disk, and both objects are orbiting within a low-density binary cavity surrounded by a circumbinary disk (CBD). The radius of the cavity from the binary center of mass to the inner edge of the CBD is equal to $2s$ (e.g., A. I. MacFadyen & M. Milosavljević 2008; C. Roedig et al. 2011).

We assume both mini-disks are fixed to their central SMBHs and are co-aligned with the binary orbital plane,

extending radially from $r_{\text{in}} = 1.5 r_g$ (the innermost stable circular orbit; ISCO) to r_{out} , where both minidisks are tidally truncated due to orbital resonances in the binary orbital cavity (J. Papaloizou & J. E. Pringle 1977; D. N. C. Lin & J. Papaloizou 1979; B. Paczynski & B. Rudak 1980; C. Roedig et al. 2014). As opposed to the accretion disk of an isolated SMBH, SMBH binaries evolve in a time-dependent gravitational potential that truncates the attached mini-disks by destabilizing particle orbits in the binary cavity. Following B. Pichardo et al. (2005), the outermost stable particle orbit of the SMBHs in a circular binary are

$$r_{\text{out}} \approx 0.733 \left(\frac{q}{1+q} \right)^{0.07} r_{\text{L}}, \quad (3)$$

where r_{L} is the Roche lobe radius of each SMBH (P. P. Eggleton 1983). For example, $r_{\text{out}} \approx 0.62 r_{\text{L}} - 0.70 r_{\text{L}}$ for a range of mass ratios between $q = 0.1$ and 1, respectively. At the same time, the Roche lobe radius of the primary (secondary) SMBH varies between $0.58 r_{\text{L}} - 0.38 r_{\text{L}}$ ($0.21 r_{\text{L}} - 0.38 r_{\text{L}}$), respectively.

2.2. Accretion Rates

Gas supplied by the CBD flows at a steady rate \dot{M} onto the minidisks' outer edges. The accretion rates onto the primary and secondary SMBHs of the binary, \dot{m}_1 and \dot{m}_2 (where $\dot{M} = \dot{m}_1 + \dot{m}_2$), depend on the mass ratio q with the larger accretion rate corresponding to the lighter SMBH. This effect, known as accretion inversion (P. Artymowicz & S. H. Lubow 1994; R. Günther & W. Kley 2002; K. Hayasaki et al. 2007; C. Roedig et al. 2011; B. D. Farris et al. 2015), occurs because the lighter SMBH orbits closer to the inner rim of the CBD. L. Z. Kelley et al. (2019) describe this effect by fitting the simulation data of B. D. Farris et al. (2015), finding

$$\dot{m}_2 = \dot{m}_1 \left(\frac{50}{(12q)^{3.5} + (12q)^{-3.5}} \right). \quad (4)$$

We adopt this description in our calculation and further assume that \dot{m}_1 and \dot{m}_2 are constant during the binary orbit, for simplicity.

The total accretion rate onto the binary is characterized by its Eddington ratio,

$$\lambda_{\text{tot}} = \frac{\dot{M}}{\dot{M}_{\text{Edd,tot}}}, \quad (5)$$

where $\dot{M}_{\text{Edd,tot}} = (2.2 \times 10^{-8} M_{\odot} \text{ yr}^{-1})(0.1/\varepsilon_{\text{rad}})(M/M_{\odot})$ and the radiative efficiency⁴ ε_{rad} is 0.1. The Eddington ratios of the

primary and secondary are therefore $\lambda_1 = \dot{m}_1/\dot{M}_{\text{Edd,1}}$ and $\lambda_2 = \dot{m}_2/\dot{M}_{\text{Edd,2}}$. Defining $\kappa = \dot{m}_2/\dot{m}_1$, expressions for λ_1 and λ_2 can be derived in terms of κ , q and λ_{tot} :

$$\lambda_1 = \frac{1+q}{1+\kappa} \lambda_{\text{tot}} \quad (6)$$

and

$$\lambda_2 = \frac{1+q}{q} \frac{\kappa}{1+\kappa} \lambda_{\text{tot}}. \quad (7)$$

As κ is only a function of q , the Eddington ratios onto both SMBHs are determined by specifying q and λ_{tot} , and are independent of the total mass of the binary M .

Color maps of λ_1 and λ_2 in the $(q, \lambda_{\text{tot}})$ plane are shown in Figure 1. The effects of accretion inversion are clearly seen in the figures, and are most acute when $q \lesssim 0.1$ and the secondary is orbiting close to the inner edge of the CBD. In this scenario, λ_2 can be driven into the super-Eddington regime even if $\lambda_{\text{tot}} \sim 0.1$. The strong variation of the Eddington ratios across the parameter space impacts the likelihood of observing a significant X-ray reflection signal from a potential binary and results in a wide range of ionization conditions. X-ray reflection from the inner accretion disk requires the presence of Compton-thick gas. When Eddington ratios get too low ($\lesssim 0.01$) or too high ($\gtrsim 1$), accretion disks are expected to become geometrically thick and thus less dense (e.g., O. Blaes 2014), and less susceptible to producing an X-ray reflection spectrum. We therefore focus (with one exception) on $(q, \lambda_{\text{tot}})$ values where the Eddington ratios for both SMBHs are between 0.01 and 1 and a geometrically-thin, optically-thick accretion disk is likely to exist around each object. The specific values chosen are indicated by the letters in Fig. 1 and are shown in Table 1.

Configuration (a) does have $\lambda_2 = 2.3$, but as this is only slightly super-Eddington we include it in our sample in order to consider uniform coverage of the $(q, \lambda_{\text{tot}})$ plane.

2.3. X-ray Reflection Calculation

The accretion disk around each SMBH in the binary is assumed to be irradiated by a static, hard X-ray emitting corona located $10 r_g$ above the black hole (i.e., a ‘lamppost’ corona; e.g., A. Martocchia & G. Matt 1996; T. Dauser et al. 2013). We neglect any X-ray flux from the corona of the primary that may strike the disk of the secondary (and vice versa). The relativistic ionized X-ray reflection spectrum from each accretion disk is com-

Znajek 1977), we adopt a value of 0.1, consistent with observations of AGNs (e.g., S. W. Davis & A. Laor 2011). A larger value of ε_{rad} would result in rescaling of the mini-disk ionization parameters by the same factor and consequently, we do not expect it to have a significant impact on our results.

⁴ While the maximum possible radiative efficiency for a SMBH with spin $a = 0.99$ is ≈ 0.4 (e.g., R. D. Blandford & R. L.

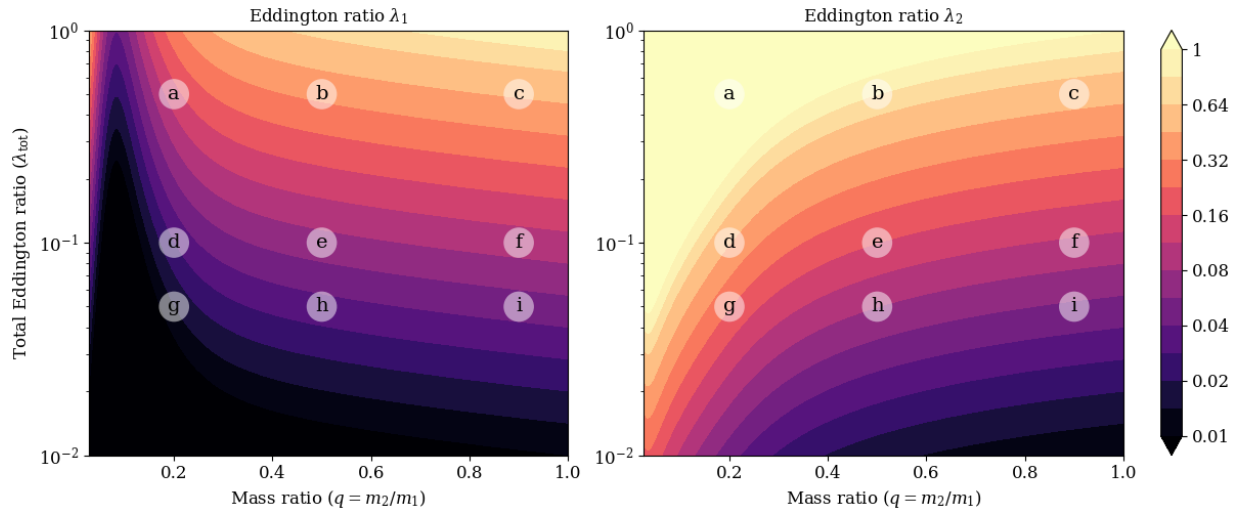


Figure 1. The color map shows the individual Eddington ratios for the primary (left) and secondary (right) SMBHs as a function of binary mass ratio ($q = m_2/m_1$) and the total Eddington ratio onto the binary (λ_{tot} ; Eq. 5). The accretion inversion phenomenon is easily seen in these plots, in particular at $q \lesssim 0.1$ where $\lambda_1 < 0.01$ and λ_2 is super-Eddington even if $\lambda_{\text{tot}} \sim 0.1$. The letters correspond to specific model parameters discussed in Sect. 3 and Table 1.

Table 1. Eddington ratios and peak disk ionization parameters for each SMBH binary configuration considered in Sect. 3. The letters correspond to the locations marked in Figs. 1 and 2.

	λ_{tot}	q	λ_1	$\log(\xi)_1$	λ_2	$\log(\xi)_2$
(a)	0.5	2/10	0.14	2.90	2.30	6.01 [†]
(b)	0.5	5/10	0.35	3.94	0.80	4.87 [†]
(c)	0.5	9/10	0.47	4.28	0.53	4.41
(d)	0.1	2/10	0.03	0.98	0.46	4.26
(e)	0.1	5/10	0.07	2.09	0.16	3.07
(f)	0.1	9/10	0.09	2.45	0.11	2.59
(g)	0.05	2/10	0.01	0.13	0.23	3.48
(h)	0.05	5/10	0.04	1.26	0.08	2.26
(i)	0.05	9/10	0.05	1.62	0.05	1.77

NOTE—[†] Replaced with 4.70 for calculation with the `relxillpCp` model.

puted using the `relxillpCp` model (e.g., T. Dauser et al. 2016) within `Xspec` (K. A. Arnaud 1996). As described in Sect. 2.1, the SMBH spins are fixed at $a = 0.99$ and the disks extend from r_{in} to r_{out} (Eq. 3). Each corona has an electron temperature of 60 keV and produces a Comptonization spectrum with photon-index $\Gamma = 2$, consistent with values commonly observed from single AGNs (e.g., A. C. Fabian et al. 2015). We assume a disk inclination of 30 degrees (we discuss the emission geometry in more detail in Section 2.4) and adopt Solar abundances.

The strength of the spectral features in reflection spectra, including the Fe $K\alpha$ line, are strong functions of the ionization state of the gas at the surface of the accretion disk (e.g., R. R. Ross & A. C. Fabian 2005; J. García & T. R. Kallman 2010). If the disk surface is strongly illuminated and becomes highly ionized, then it becomes effectively a mirror, reflecting the irradiating spectrum outwards, augmented with only very weak and highly Comptonized spectral features. The properties of a reflection spectrum can be described using the ionization parameter, $\xi = 4\pi F_X/n_H$, where F_X is the X-ray flux irradiating gas with hydrogen number density n_H . Gas with $\log \xi \gtrsim 4$ is considered highly ionized and yields very weak reflection features (e.g., J. García & T. R. Kallman 2010).

A central compact corona, such as the lamppost model, will produce a radially dependent $F_X(r)$ (e.g., K. Fukumura & D. Kazanas 2007; T. Dauser et al. 2013) which, when combined with the density profile $n_H(r)$, will generate an ionization gradient across the disk (e.g., D. R. Ballantyne 2017). The total reflection spectrum from each mini-disk is found by integrating the reflection spectra over disk radii, taking into account the relativistic shifts that blur the spectra at each radius (e.g., A. C. Fabian et al. 1989). As the inner disk is more strongly illuminated than the outer disk, the ionization parameter at the inner edge is crucial in determining the properties of the total reflection spectrum.

The `relxillpCp` model includes the effects of this ionization gradient (assuming a N. I. Shakura & R. A. Sunyaev 1973 radial density profile) when calculating the total relativistic reflection spectrum of each mini-

disk. The density at the inner edge of each disk is set to 10^{15} cm^{-3} (the impact of this assumption is discussed in Sect. 5.3). The peak ionization parameter at a distance $(11/9)^2 r_{\text{in}}$, denoted ξ_1 and ξ_2 , must also be specified for each mini-disk. These values are computed using the analytical ionization gradient formula for a lamp-post corona derived by D. R. Ballantyne (2017). This formula depends on the Eddington ratio of each mini-disk, the radiative efficiency (set to 0.1, as before), the Shakura-Sunyaev α -parameter (set to 0.1), and is independent of SMBH mass. The D. R. Ballantyne (2017) equation also makes use of the coronal dissipation fraction f_X (R. Svensson & A. A. Zdziarski 1994) to convert from the bolometric luminosity, powered by accretion, to the X-ray flux. Here, we connect f_X to the X-ray bolometric correction, k_X , via $f_X = 1/k_X$, and use the F. Duras et al. (2020) fitting formula to calculate k_X at the Eddington ratio of each mini-disk.

The resulting values of $\log \xi_1$ and $\log \xi_2$ computed using the D. R. Ballantyne (2017) formula are shown as functions of q and λ_{tot} in Figure 2. The color maps show the impact of the accretion inversion effect on the ionization parameters, which is exacerbated by the strong dependence of ξ on λ predicted by the D. R. Ballantyne (2017) equation ($\xi \propto \lambda^3$). As a result, the ionization state of the mini-disks will change by orders of magnitude in response to only moderate differences in q or λ_{tot} . This will lead to a wide range of possible Fe K α line strengths and shapes, as well as other reflection signatures, in the composite spectra of SMBH binaries, especially when $q \lesssim 0.4$. The accretion inversion also causes the mini-disk of the secondary SMBH to be more highly ionized than the primary mini-disk. The letters on the plots show the 9 (q, λ_{tot}) locations from Fig. 1 and the associated $\log \xi_1$ and $\log \xi_2$ values are found in Table 1. The peak ionization parameters span the range from $\log \xi = 0.05$ to > 5 ; however, the maximum $\log \xi$ allowed by `relxillpCp` is 4.70, so any peak ionization parameter $> 10^{4.7}$ is replaced with this value. In practice, once the illuminated gas is fully ionized (at $\log \xi \gtrsim 4$; J. García & T. R. Kallman 2010), there is little difference in the predicted reflection spectra for any higher value of ξ . Therefore, the use of the $\log \xi = 4.7$ upper-limit will not affect the properties of the predicted SMBH binary spectra.

Now armed with the values of $\log \xi_1$ and $\log \xi_2$, `relxillpCp` models can be computed for each mini-disk in the binaries listed in Table 1. In addition to the parameters already described, we set the redshifts to zero, allow for the effects of returning radiation (T. Dauser et al. 2022), and include the correct contribution from the continuum in a lamp-post geometry (i.e.,

`refl_frac=1` and `switch_reflfrac_boost=1`). For plotting purposes, all spectra are computed from 0.02–200 keV in 2000 logarithmically spaced bins.

2.4. Emission Geometry and Calculation of the Composite Spectra

At this stage, we have calculated the relativistic ionized reflection spectrum from the mini-disks of 9 SMBH binary configurations described by the (q, λ_{tot}) parameters in Table 1. However, each SMBH in a binary will be moving relative to each other, leading to velocity shifts that must be taken into account when combining the two X-ray spectra to form the composite. We therefore must specify details of the geometry of the SMBH binaries in order to account for these velocity shifts.

Our chosen geometry is depicted in Figure 3. Both mini-disks are coplanar with the binary orbital plane. The inclination i is defined as the angle between the line of sight $\hat{\mathbf{o}}$ (defined as originating from the binary center of mass and pointing to the observer) and the binary orbital angular momentum vector $\hat{\mathbf{z}}$ (normal to the binary orbital plane). If $i \in [-90^\circ, 90^\circ]$, then $\hat{\mathbf{o}} \cdot \hat{\mathbf{z}} > 0$, and the orbit appears counterclockwise, and vice-versa. The phase angle f takes on values from 0 to 360° . Conjunction, when both orbital velocities are completely perpendicular to $\hat{\mathbf{o}}$, happens at $f = 0^\circ$ (defined as the point at which the primary black hole crosses the $+\hat{\mathbf{x}}$ -axis) and $f = 180^\circ$, when the secondary is the one crossing the $+\hat{\mathbf{x}}$ axis. In both cases, the orbital Doppler effect is minimal (but non-zero, as we take into account a transverse Doppler effect). Conversely, the opposition is defined as the two points when the BH velocities projected onto the line of sight are at their maximum. The secondary moves towards the observer at $f = 90^\circ$, and away from it at $f = 270^\circ$. The opposite is true for the primary. The more “edge-on” the binary is (i close to 90°), the more pronounced the Doppler shift on both spectra is expected to be. As with the `relxillpCp` models described in Section 2.3, we adopt the inclination angle $i = 30^\circ$. We defer an investigation of a wider range of inclinations to a future study and note that the adopted value affects both the relativistic blurring of spectral features and the apparent velocity offset of the two SMBHs.

The orbital speed of each of the two SMBHs relative to the binary center of mass is

$$v_1 = \frac{q}{1+q} v \quad \text{and} \quad v_2 = \frac{1}{1+q} v, \quad (8)$$

where $v = \sqrt{GM/s}$ is the relative orbital speed of the two SMBHs in a circular Keplerian orbit, which is equal to $0.1c$ for $s = 100 r_g$. The Doppler factor depends on the fraction of the orbital velocity that is parallel to the

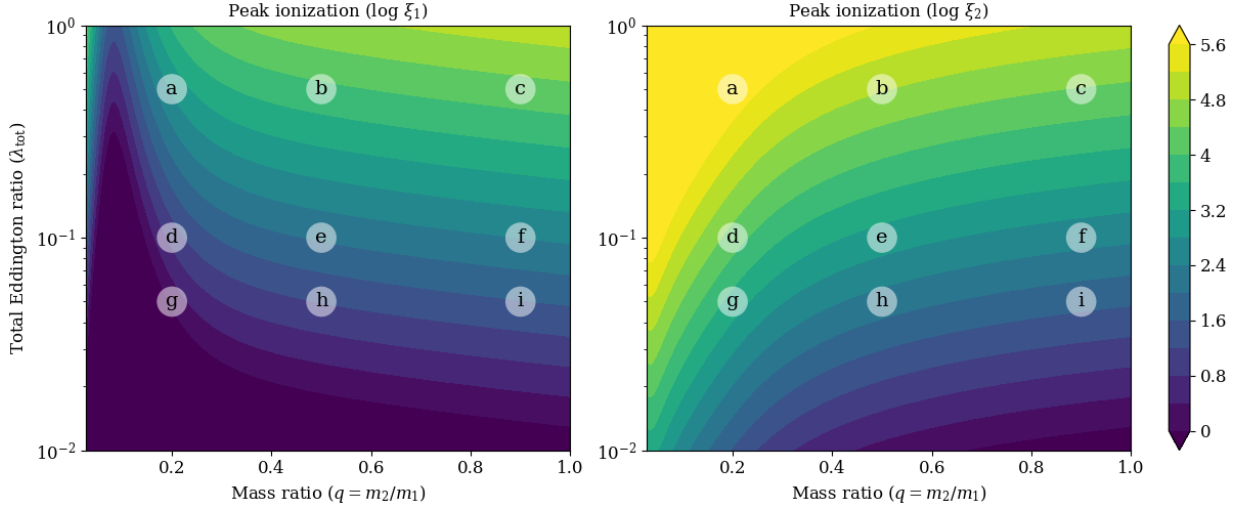


Figure 2. The color maps show the peak ionization parameter in the mini-disks around the primary ($\log \xi_1$; left panel) and secondary ($\log \xi_2$; right panel) SMBHs in the $(q, \lambda_{\text{tot}})$ plane. The ionization parameters are calculated using the [D. R. Ballantyne \(2017\)](#) ionization gradient formula evaluated at a radius of $(11/9)^2 r_{\text{in}}$, which are then input to `relxillpCp` to compute the relativistic ionized reflection spectrum emitted by each mini-disk. The accretion inversion phenomenon, combined with the λ^3 dependence of the [D. R. Ballantyne \(2017\)](#) equation, causes a large variation of $\xi_{1,2}$ through the parameter space with the mini-disk of the secondary expected to be more highly ionized than the primary. The values of $\log \xi_1$ and $\log \xi_2$ at the location of the letters in the plots are listed in Table 1.

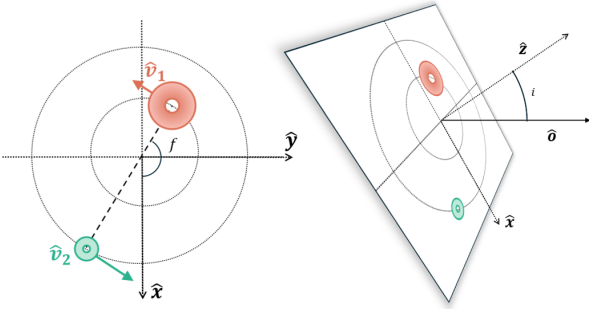


Figure 3. Illustration of the binary emission geometry. The SMBHs are on concentric circular orbits on the xy -plane, where \hat{x} is defined as the projection of the \hat{o} vector (from binary center of mass to the observer) onto the binary orbital plane. \hat{z} is defined as the angular momentum vector of the binary, perpendicular to the plane and forming an angle i with the observer vector. The orbital phase f is defined as the angle between the \hat{x} axis and the primary black hole.

line of sight, $\vec{v}_{1,2} \cdot \hat{o} = \pm |\vec{v}_{1,2}| \sin i \sin f$:

$$1 + z_{\text{orb}} = \frac{\sqrt{1 - (v_{1,2}/c)^2}}{1 \pm (v_{1,2}/c) \sin i \sin f} \quad (9)$$

where, because we have defined f around the location of the secondary BH, we take the negative value when computing the primary's Doppler shift. These orbital redshifts are implemented using the `zshift` function in `Xspec`.

The final step before computing the total spectrum of a binary is to renormalize the individual spectra from each mini-disk to account for the relative sizes and accretion-powered luminosities of the disks. The `relxillpCp` model produces spectra in units of flux defined per unit area of the emitting surface. Therefore, the relative contribution to the total luminosity of the secondary's mini-disk relative to that of the primary is defined as $\kappa (r_{\text{out},2}^2 - r_{\text{in},2}^2) / (r_{\text{out},1}^2 - r_{\text{in},1}^2)$. With the relative normalizations and velocity shifts now determined, the composite X-ray spectra from each of the 9 binary configurations in Table 1 can be calculated at any orbital phase.

3. COMPOSITE X-RAY REFLECTION SPECTRA OF SMBH BINARIES

Figure 4 shows the relativistic ionized reflection spectra from the mini-disks around the primary (dashed lines) and secondary (dot-dashed lines) SMBHs, along with the summed composite spectra (solid lines) from the 9 binaries listed in Table 1. The plotted spectra are calculated when each binary is at opposition (i.e., $f = 90^\circ$; Fig. 3), which maximizes the line-of-sight velocity difference between the two SMBHs. As our focus is to study the reflection properties of SMBH binaries, the effects of ionized and neutral absorption, which are commonly observed in AGNs (e.g., [C. Ramos Almeida & C. Ricci 2017](#)), as well as any soft X-ray emission from a warm corona (e.g., [D. R. Ballantyne 2020](#)), are omitted.

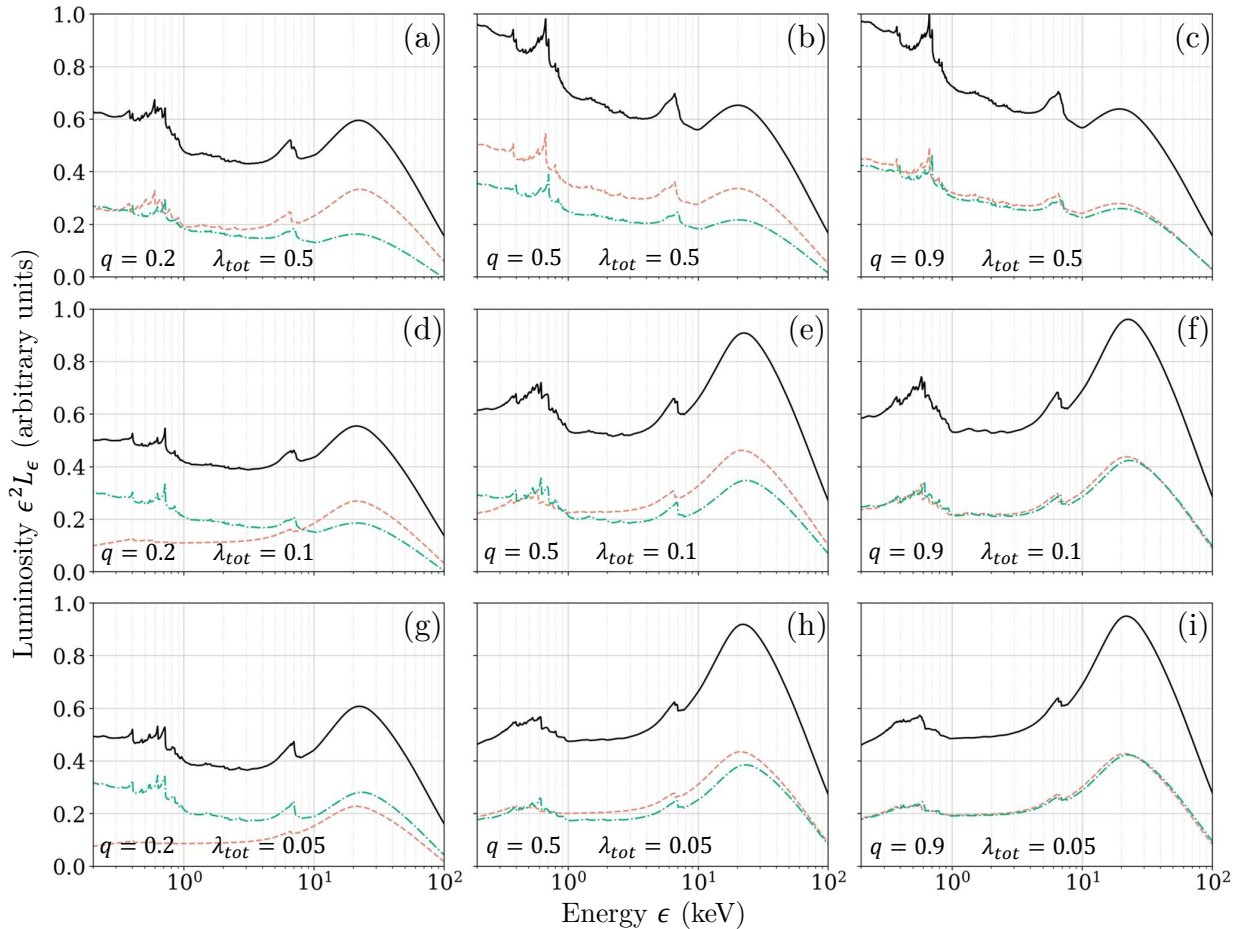


Figure 4. Total relativistic ionized reflection spectra from the 9 SMBH binary configurations shown in Table 1 (solid lines). All are calculated for binaries in opposition ($f = 90^\circ$) and the inclination of the observer $i = 30^\circ$. The reflection spectra from the mini-disks around the primary and secondary SMBHs are shown as the dashed and dot-dashed lines, respectively. The y-axis has been scaled for each λ_{tot} to show the spectra over the same relative range. When $q = 0.9$, the two mini-disks produce very similar spectra which combine to accentuate the reflection features in the total spectrum. Unequal mass binaries are however impacted by the accretion inversion effect which causes the two mini-disks to have very different reflection properties.

Each row of Fig. 4 is scaled so that the effects of increasing q are easily seen for each λ_{tot} . When $q = 0.9$, the two SMBHs are of near equal mass and are accreting at approximately the same rates. As a result, both mini-disks are about the same size and at very similar ionization states (Table 1). The resulting reflection spectra from the two mini-disks are therefore nearly identical (panels (c), (f) and (i) in Fig. 4). This leads to a total binary spectrum with more prominent reflection features, with stronger emission lines and Compton hump (at ≈ 20 keV) than the spectra from either of the mini-disks. However, the composite spectra are still dominated by features from a small range of ionization parameters.

The effects of the accretion inversion phenomenon become stronger as q decreases. As m_2 and m_1 become more unequal, so do the individual accretion rates, with the secondary accreting more rapidly than the primary,

leading to a more highly ionized disk (see Table 1). When $q = 0.2$ the peak ionization parameter of the secondary can be well over an order of magnitude larger than the primary (Fig. 2). As a result, the composite spectra of these binaries show features from a mix of ionization states. Unlike the high q case, the impact on the composite can be limited to only a portion of the spectrum, depending on the value of q and λ_{tot} . For example, in panels (a) and (e), the soft X-ray emission lines below $\lesssim 1$ keV are strongly affected by the sum of different reflection features, while in panels (d) and (g), the impact is strongest for the Compton hump. These results show that evidence for a SMBH binary may sometimes be found in only a part of an observed X-ray spectrum, and not exclusively in the Fe K α line.

In general, a larger λ_{tot} leads to a higher accretion rate and therefore a more highly ionized mini-disk around both SMBHs (Fig. 2). Because of the accretion inver-

sion effect, the mini-disk around the primary is very weakly ionized when $\lambda_{\text{tot}} = 0.05$. At these low ionization levels, the reflection spectrum is impacted by absorption (J. García & T. R. Kallman 2010), and the predicted spectra from the mini-disk are dominated by the contribution from the $\Gamma = 2$ continuum, along with a relatively weak relativistically broadened Fe $K\alpha$ line (see, e.g., panel (g) in Fig. 4). At larger values of ξ_1 and ξ_2 , the reflection spectra from the mini-disks contain both a relativistic Fe $K\alpha$ line from the inner disk and a number of soft X-ray lines from larger radii due to the ionization gradient across the disk. Crucially, even scenarios when the inner disk is nearly completely ionized (e.g., the secondary mini-disk in panels (a)-(c) in Fig. 4), the ionization gradient still produces an Fe $K\alpha$ line and soft X-ray features from reflection at larger radii along the disk. Moreover, in most configurations shown in Fig. 4 the composite spectra exhibit visibly double-peaked Fe $K\alpha$ line profiles, which are of interest as a potentially unique signature of SMBH binaries.

As mentioned above, Fig. 4 shows the SMBH reflection spectra at opposition ($f = 90^\circ$) where there is the largest relative velocity between the two SMBHs. At the assumed distance of $100 r_g$, the shift generates changes to the total binary spectra, especially around the Fe $K\alpha$ line and other narrow features in the soft end. The magnitude of the special relativistic Doppler shift for both SMBHs add up to $|z| = 0.082$ for the assumed orbital inclination of $i = 30^\circ$ (and is at most $|z| = 0.095$ for edge-on orientation). Figure 5 illustrates how the composite Fe $K\alpha$ line profile from binary (d) changes as a function of the orbital phase at $f = 90^\circ, 135^\circ, 180^\circ, 225^\circ$ and 270° . The modeled emission-line profile exhibits a visible change in shape, by evolving from double-peaked (for $f = 90^\circ$) to a single-peaked profile. It also shows a shift of the blue edge of the emission line profile by about 0.5 keV, consistent with the expected orbital Doppler shift due to the orbital motion of the brighter secondary.

In this example, the two mini-disks of the binary have very different ionization patterns. Due to the accretion inversion effect, the secondary SMBH is accreting rapidly and has a mini-disk that is very highly ionized at its inner edge. As a result, its Fe $K\alpha$ line comes from ionized iron at larger radii and the line profile is moderately broadened. In contrast, the primary SMBH is accreting weakly and the mini-disk is weakly ionized at the inner edge. Its reflection spectrum, therefore, exhibits a very relativistically broadened neutral (or weakly ionized) Fe $K\alpha$ line. The addition of this broad, low-contrast feature to the narrower ionized one from the mini-disk of the secondary produces modest changes to the composite line of the binary. However,

the low ionization state of the primary’s mini-disk gives its reflection spectrum a harder slope than the one from the secondary’s mini-disk. Indeed, the spectrum from the primary SMBH dominates the composite at energies > 8 keV.

4. OBSERVATIONAL PROSPECTS

The previous section shows that the predicted reflection spectra of SMBH binaries could be strongly impacted by the mass ratio q and total Eddington ratio λ_{tot} of the binary. At large q , the total binary spectrum will have strong reflection features due to the addition of two very similar spectra from the mini-disks. However, when $q \lesssim 0.5$, the individual reflection spectra may be very different due to the accretion inversion effect, and the evidence of a binary may be isolated to only certain regions of the total spectrum. In this Section, we perform a limited investigation of the observational prospects for detecting evidence of a SMBH binary from a typical long X-ray observation. A more thorough study that considers a wider range of binaries and observational strategies is deferred to a future paper.

4.1. Setup

We simulate 100 ks observations of the composite X-ray spectrum from a SMBH binary with $q = 0.9$ and $\lambda_{\text{tot}} = 0.1$ (i.e., binary (f); Table 1) at $z = 0.1$ and at $z = 1.0$. This configuration is chosen because both mini-disks produce clear reflection signatures across a wide range in energy. The total mass of the binary is either $10^9 M_\odot$ or $10^6 M_\odot$, referred to as a ‘PTA’ or ‘LISA’ binary, respectively. The rest-frame 2–10 keV X-ray flux of each mini-disk is

$$F_{2-10\text{keV}} = f_X \frac{\lambda L_{\text{Edd}}}{4\pi d_L^2(z)}, \quad (10)$$

where f_X is the F. Duras et al. (2020) bolometric correction evaluated at the appropriate Eddington ratio λ for the mini-disk, and L_{Edd} is the Eddington luminosity for the primary or secondary SMBH. A Λ CDM cosmology with $H_0 = 70 \text{ km s}^{-1} \text{ Mpc}^{-1}$, and $\Omega_m = 0.3$ is used to compute the luminosity distance d_L to redshift z . The resulting fluxes of the primary and secondary mini-disks are then fixed using the `cflux` command in `Xspec`. Absorption from a Galactic column density of $N_{\text{H}} = 3 \times 10^{20} \text{ cm}^{-2}$ is applied to the spectra of both mini-disks using the `phabs` model. Figure 6 shows the model spectrum for a $z = 0.1$ PTA binary with $f = 90^\circ$.

It is interesting to note that the exposure time (here adopted to be 100 ks ≈ 1.2 days) is comparable to or larger than the orbital time of a LISA binary with a separation close to $100 r_g$ (see equation 1). The resulting

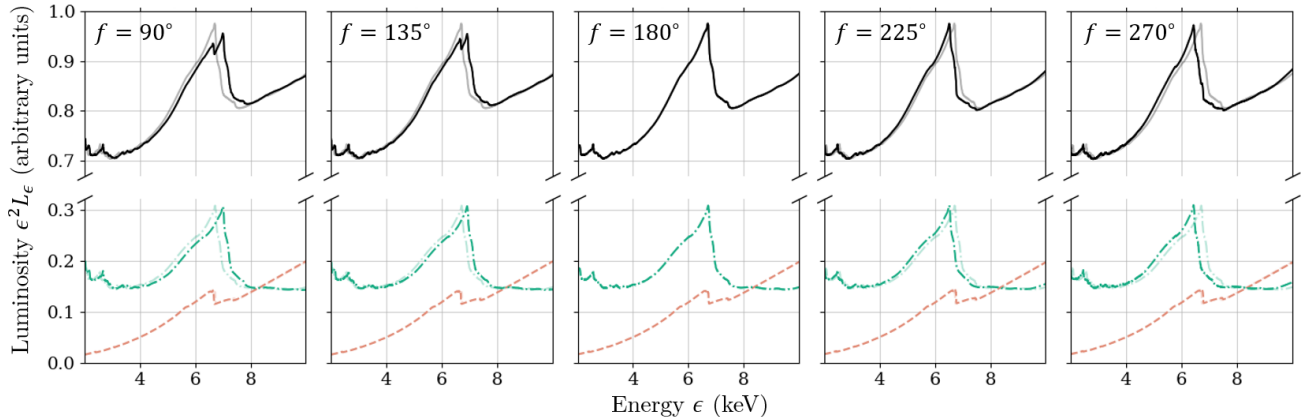


Figure 5. The effect of binary motion on the total Fe $K\alpha$ line profile from a SMBH binary at inclination $i = 30^\circ$ with $q = 0.2$ and $\lambda_{\text{tot}} = 0.1$ (i.e., binary (d); Table 1). The line styles are the same as in Fig. 4. The panels show the Fe $K\alpha$ line profile at $f = 90^\circ$ (opposition; brighter secondary moving towards the observer), $f = 135^\circ$, $f = 180^\circ$ (conjunction), $f = 225^\circ$ and $f = 270^\circ$ (opposition; brighter secondary moving away from the observer). Each panel includes the profiles of the $f = 0^\circ = 180^\circ$ binary (with no orbital offset) as a semi-transparent curve for visual comparison. The relative motion of the two SMBHs leads to noticeable changes in the shape and offset of the Fe $K\alpha$ line profile.

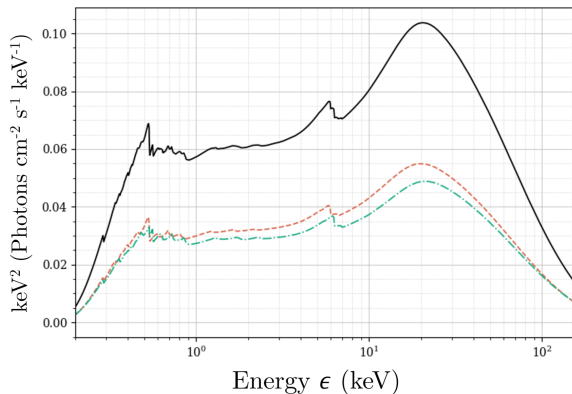


Figure 6. The X-ray spectral model used to simulate a 100 ks observation of a SMBH binary candidate. The line styles are the same as Fig. 4. The binary considered has $q = 0.9$ and $\lambda_{\text{tot}} = 0.1$ (i.e., binary (f); Table 1) and is shown at $z = 0.1$ and at a phase angle of 90° . Galactic absorption with column density of $3 \times 10^{20} \text{ cm}^{-2}$ is applied to the model, which was not the case for models from Sect. 3.

X-ray spectrum detected from such binaries would then effectively be orbit-averaged. To account for this effect, we average the model spectrum of the *LISA* binary over the full orbit to capture the smearing due to the time-dependent orbital Doppler shifts. That is, we average over the binary orbit’s 4 extremal points: conjunction at $f = 0^\circ$ and 180° , and opposition at $f = 90^\circ$ and 270° . Conversely, the 100 ks exposure time is much shorter than the months-long orbital period of a PTA binary which results in a snapshot of the spectrum at a fixed phase. The model for PTA binaries is set at opposition ($f = 90^\circ$) when the orbital shifts are most prominent for both SMBHs.

We simulate on-axis observations of the *LISA* and PTA binaries with four X-ray mission concepts that all had the potential to be operating at the same time as *LISA: NewAthena* (M. Cruise et al. 2025), *AXIS* (A. Ford et al. 2024), *HEX-P* (K. K. Madsen et al. 2024), and *STROBE-X* (P. S. Ray et al. 2024). The latter two concepts both contain two instruments that observe simultaneously and yield broadband spectra extending from below 0.5 keV to past 30 keV. While neither concept is currently being developed, it remains valuable to evaluate the potential usefulness of hard X-ray instruments in identifying SMBH binaries. *NewAthena* also has two instruments, but observations are only made with one at a time, so we simulate separate observations with either the Wide Field Imager (WFI) or the X-ray Integral Field Unit (X-IFU). *AXIS* and *NewAthena* are both sensitive from ≈ 0.2 to ≈ 12 keV, and *STROBE-X* has the largest collecting area of the four concepts, followed by *NewAthena*. Table A1 lists the specific response, ancillary and background files used to produce our simulated observations from the four telescopes. The energy resolution of the simulated spectra are determined by the response files provided by each observatory. For reference, we also include Table A2, where we indicate the nominal bandpass and collecting area at 6 keV of each instrument. All simulations are performed with *fakeit* in *Xspec* and the resulting spectra are grouped to have a minimum of 20 counts per bin.

Our goal is to emulate the process of fitting a spectrum from an unknown AGN under the hypothesis that it is emission from a single SMBH, where the observer knows only the Galactic column density in the direction of the source and the redshift of the object. Therefore, the sim-

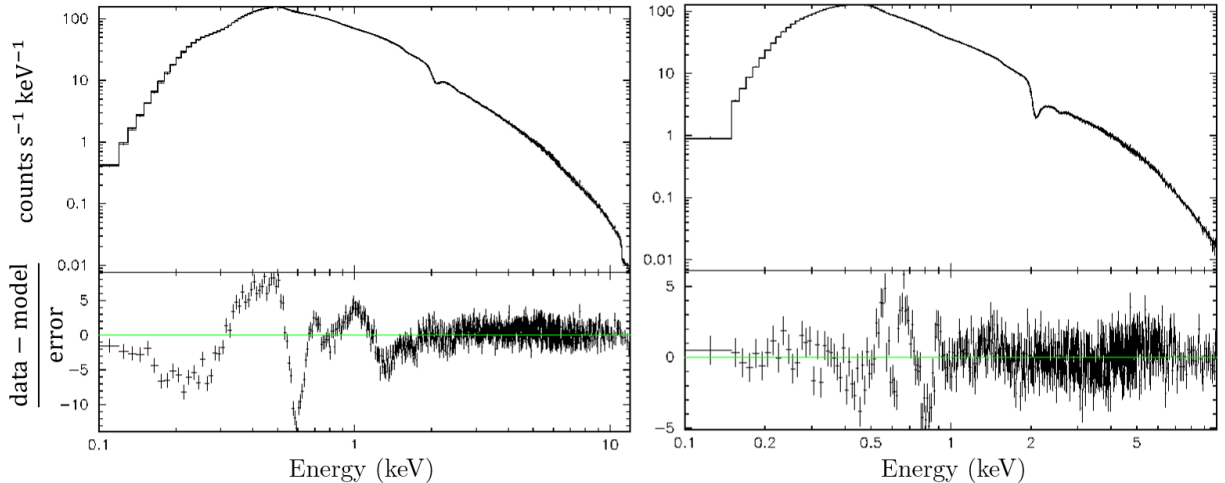


Figure 7. Left: The upper-panel shows the predicted count rate spectrum of a $z = 0.1$ PTA SMBH binary (with total mass $M = 10^9 M_{\odot}$, $q = 0.9$ and $\lambda_{\text{tot}} = 0.1$) observed by *NewAthena* (WFI) for 100 ks. The lower-panel shows the residuals when this spectrum is fit by a spectral model for a single AGN (`phabs*relxill`). Strong soft X-ray residuals are present due to the combination of emission features from the two mini-disks. Right: As in the left-hand panel but now showing the result from the simulated *AXIS* observation.

ulated spectra are fit in `Xspec` using a `phabs*relxill` model with the column density fixed at $3 \times 10^{20} \text{ cm}^{-2}$ and the redshift is set to either 0.1 or 1. Within `relxill`, the disk emissivity⁵ is set to -3 , the inner disk radius is fixed at the ISCO, the outer radius is frozen at $400 r_g$ and the inclination angle is set to 30° . The remaining `relxill` parameters (SMBH spin a , photon index Γ , ionization parameter $\log \xi$, iron abundance A_{Fe} and reflection fraction f_{refl}) are all left free to vary when fitting the simulated spectra. Goodness of fit is determined using χ^2 statistics, and uncertainties on the fit parameters are reported using a $\Delta\chi^2 = 2.71$ criterion, or a 90% confidence interval for one parameter of interest. Prior to fitting, we ignore any channels that are background dominated. Therefore, some fits, especially those for models $z = 1$, are performed over a narrower energy range than the native energy sensitivity of the instrument.

4.2. Fit Results

We examine the fit results to search for evidence of the SMBH binary in the simulated spectrum. This evidence could manifest as a poor fit (i.e., a $\chi^2/\text{d.o.f.} > 2$, where d.o.f. = degrees of freedom), or the fit could be acceptable, but one or more parameters may yield an unusual or unexpected result. A third possibility is that the fit and parameters may be reasonable, but residuals may remain that could be difficult to explain using con-

ventional AGN phenomenology. We are also interested in determining if one of the 4 X-ray observatories is best suited to finding evidence for SMBH binaries.

The fit results for our simulated PTA ($10^9 M_{\odot}$) binaries are shown in Table 2. As a reminder, the models used in the simulations all have $\Gamma = 2$, $A_{\text{Fe}} = 1$ in solar units and $a = 0.99$. There is a significant distinction in the results between a source at $z = 0.1$ (with a 2–10 keV flux of $F = 2.61 \times 10^{-11} \text{ erg cm}^{-2} \text{ s}^{-1}$) and one at $z = 1$ ($F = 1.28 \times 10^{-13} \text{ erg cm}^{-2} \text{ s}^{-1}$). All 5 simulated observations of the $z = 1$ binary are well fit with the simple single AGN model indicating that the effects of the two reflection signals are not leading to any significant residuals. However, there are hints in the values of the fit parameters that there are aspects of the simulated spectra that are not well described with one `relxill` model. In particular, the fitted SMBH spin a is almost entirely unconstrained in all 5 observations. Only the X-IFU observation gets close to the ‘true’ value of $a = 0.99$, but with a large negative error-bar. This result indicates that shape of the Fe $K\alpha$ line in the model spectrum does not match that expected from a single AGN and the fit becomes insensitive to its spin value.

The high energy sensitivity of *HEX-P* and *STROBE-X* also provide some clues for the presence of a binary at $z = 1$. In both cases, the fits return a much harder Γ than the input value, along with a low iron abundance and a large and poorly constrained reflection fraction (f_{refl}). These observatories would have the capability to detect the stronger than ‘expected’ Compton reflection hump that arises from the combination of two reflection signals (Fig. 6). Of the other observatories, only the

⁵ The standard model for `relxill` does not make any pronouncements as to the nature or geometry of the corona, and uses a simple empirical power-law to model disk emissivity.

Table 2. Best fit parameters when a `phabs*relxill` model is applied to a simulated PTA binary spectrum at opposition ($M = 10^9 M_\odot$, $q = 0.9$, $\lambda_{\text{tot}} = 0.1$, and $f = 90^\circ$). The composite binary spectrum is subject to Galactic absorption ($N_{\text{H}} = 3 \times 10^{20} \text{ cm}^{-2}$) and placed at either $z = 0.1$ or 1 (Fig. 6). Individual faked spectra are generated for 100 ks exposures by *NewAthena* (WFI), *NewAthena* (X-IFU), *AXIS*, *HEX-P*, and *STROBE-X*. The free parameters when fitting the `relxill` model are the spin parameter a , photon index Γ , ionization parameter $\log \xi$, iron abundance (in Solar units) and the reflection fraction f_{refl} . The redshift and absorbing column density are fixed at the known values. Uncertainties correspond to a 90% confidence range on the fit parameter. A ‘p’ in an error bar indicates that the error range pegged at the upper or lower limit of the parameter.

z	$\chi^2 / \text{d.o.f.}$	a	Γ	$\log \xi$	A_{Fe}	f_{refl}
<i>NewAthena</i> (X-IFU)						
0.1	15,816 / 12,164	$0.998^{+0.000p}_{-0.001}$	1.95 ± 0.00	2.46 ± 0.01	0.88 ± 0.02	0.86 ± 0.01
1.0	1,183 / 1,235	$0.997^{+0.001p}_{-0.633}$	$1.90^{+0.03}_{-0.04}$	$2.90^{+0.26}_{-0.22}$	$0.66^{+0.24}_{-0.16p}$	$1.08^{+1.32}_{-0.39}$
<i>NewAthena</i> (WFI)						
0.1	3,958 / 1,137	0.998	1.94	2.44	0.85	0.90
1.0	375 / 423	$0.323^{+0.675p}_{-0.567}$	$2.00^{+0.03}_{-0.01}$	$1.77^{+0.18}_{-0.77}$	$1.92^{+1.22}_{-1.12}$	$1.17^{+0.40}_{-0.26}$
<i>AXIS</i>						
0.1	1,304 / 893	$0.972^{+0.016}_{-0.018}$	2.01 ± 0.00	1.63 ± 0.02	$0.76^{+0.009}_{-0.011}$	1.22 ± 0.04
1.0	332 / 360	$0.524^{+0.474p}_{-1.523p}$	$2.00^{+0.03}_{-0.04}$	$1.73^{+0.66}_{-0.92}$	$0.50^{+3.41}_{-0p}$	$0.92^{+1.19}_{-0.36}$
<i>HEX-P</i>						
0.1	2,586 / 2,381	$0.998^{+0.000p}_{-0.010}$	1.94 ± 0.00	2.51 ± 0.04	0.84 ± 0.05	0.96 ± 0.02
1.0	160 / 201	$0.667^{+0.331p}_{-1.665p}$	1.85 ± 0.07	$3.10^{+0.21}_{-0.36}$	$0.52^{+0.38}_{-0.02p}$	$2.65^{+7.35p}_{-1.71}$
<i>STROBE-X</i>						
0.1	2,953 / 1,621	$0.987^{+0.011p}_{-0.010}$	2.01 ± 0.00	$1.64^{+0.01}_{-0.02}$	0.91 ± 0.03	$1.35^{+0.02}_{-0.03}$
1.0	535 / 536	$0.599^{+0.399p}_{-1.597p}$	$1.91^{+0.03}_{-0.04}$	$2.92^{+0.30}_{-0.34}$	$0.50^{+0.19}_{-0p}$	$0.93^{+9.07p}_{-0.25}$

X-IFU observation gives a hint of a harder spectrum, although both A_{Fe} and f_{refl} return values typical of a single AGN. The large soft X-ray sensitivity of *AXIS* allows it to find the correct Γ , but the fit value for iron abundance remains largely unconstrained with *AXIS*.

The results for a PTA binary at $z = 0.1$ are dramatically different than those at $z = 1$ as all the simulated observations (except for *HEX-P*) cannot be adequately fit by a single AGN model⁶. In fact, the *NewAthena* (WFI) fit is so poor (with $\chi^2/\text{d.o.f.} > 2$) that error-bars cannot be calculated. The reason for the poor fits is illustrated in Figure 7 which shows the results from the

mock *NewAthena* (WFI) and *AXIS* observations. In both cases, strong residuals are seen between ≈ 0.5 and 0.8 keV, indicating that the single AGN model cannot account for the combination of spectral features predicted in the composite binary spectrum. The complexity of the soft X-ray line emission predicted by the model arises from ionization gradients on both mini-disks as well as the small velocity shifts between the two SMBHs. As a result, a model that predicts the reflection spectrum from one accretion disk with a single ionization parameter is unable to reproduce the spectrum that our model predicts from the binary. Although the fits of the $z = 0.1$ PTA binary are almost all statistically poor, the resulting fit parameters are all well constrained and are close to the ‘true’ values (e.g., the SMBH spin). Interestingly, even with these high signal-to-noise spectra,

⁶ We do note that the *HEX-P* fit still shows clear residuals mostly clustered in the soft end similarly to the other instrument fits, despite a χ^2 value of ~ 1.1 .

the composite Fe K α line predicted from the binary does not produce significant residuals when fit with a single AGN model. Therefore, if they can be convincingly separated from any warm absorption or coronal emission, complex soft X-ray emission lines may be the most direct evidence for a SMBH binary in a single X-ray spectrum.

Fit results for simulated observations of a *LISA* binary ($M = 10^6 M_\odot$) are shown in Table 3. This source is 10^3 times fainter than the PTA binary (2–10 keV flux of $F = 2.61 \times 10^{-14}$ erg cm $^{-2}$ s $^{-1}$ at $z = 0.1$ and $F = 1.28 \times 10^{-17}$ erg cm $^{-2}$ s $^{-1}$ at $z = 1$) and we find that spectral analysis is impossible for such a binary at $z = 1$ with a 100 ks exposure from any of the 4 observatories. The predicted number of counts does not give enough channels above background to perform more than a rudimentary fit. While such a source is likely detectable by all the observatories and potentially identified as an AGN, detailed spectral analysis can only be done through significantly longer exposures. If a *LISA* binary is placed at $z = 0.1$, then 100 ks exposures are sufficient to perform spectral fitting for all instruments. The results are broadly consistent with those found from the $z = 1$ PTA binary discussed above: fits using a single AGN spectral model are all successful, the SMBH spin parameter is unconstrained, and *HEX-P* and *STROBE-X* show evidence of a very hard spectrum with a large iron abundance. It is notable that even with the large collecting area of *NewAthena*, exposure times $\gg 100$ ks may be needed to convincingly uncover evidence of SMBH binaries destined to be *LISA* sources.

4.3. Detecting Orbital Variability in Fe K α Line Profiles

The above discussion showed that a single X-ray observation of a source may not be sufficient to find clear evidence of a SMBH binary. However, for high mass PTA binaries, multiple X-ray observations of the same object will probe different phases of the binary orbit, and the resulting changes in the composite spectrum could be identified through spectral fitting. As shown in Fig. 5, changes in the Fe K α line profile with orbital phase could be an important indicator of the presence of a SMBH binary.

We test this possibility by simulating 100 ks *NewAthena* observations of the PTA binary shown in Fig. 5 (i.e., $M = 10^9 M_\odot$, $q = 0.2$ and $\lambda_{\text{tot}} = 0.1$) at phases of $f = 90^\circ$, 180° and 270° . The three model binary spectra are computed as in Sect. 4.2 and the source is assumed to be at $z = 0.1$. Given the high count-rate predicted for the *NewAthena* observations, we group the mock observations to have a minimum of 50 counts per bin. As our goal is to determine if the different orbital

phases can be detected in the composite Fe K α profile, we fit the mock spectra between 2 and 12 keV with a `phabs*relxill` spectral model. This energy range eliminates the possibility of soft X-ray features dominating the fitting procedure.

Table 4 shows the results for both X-IFU and WFI observations of the binary. For both instruments, the spectra from all three orbital phases are well fit by the single AGN spectral model. The largest spectrum-to-spectrum change is seen from the simulated X-IFU observation of the $f = 270^\circ$ model which yields a significantly different ionization parameter and a higher reflection fraction than for the other orbital phases. However, these types of variations in reflection parameters are not uncommon when fitting multiple observations of a single AGN (e.g., L. Keek & D. R. Ballantyne 2016), and can be interpreted as arising from the complex dynamical environment of an accretion disk corona rather than evidence for a binary. Similar to what was found with our previous simulations, all of the fits struggled to constrain the SMBH spin with values often changing drastically between orbital phases. Notably, the WFI observation of the $f = 90^\circ$ spectrum returns a negative spin parameter, while the fits to the other two phases are consistent with a typical prograde spin. Repeated X-ray observations of a source that exhibits such variability in its measured SMBH spin could indicate the presence of an unusual and changing Fe K α line profile consistent with the presence of a SMBH binary (e.g., Fig. 5).

5. DISCUSSION

5.1. Feasibility of SMBH Binary Detection Through X-ray Reflection Signatures

Our analysis points to several outcomes relevant to detection of SMBH binaries using X-ray reflection spectroscopy. One is that by themselves, the single-epoch X-ray spectra are not likely to be a smoking gun that can be used to decisively diagnose a binary. They can however provide supporting evidence for it by indicating that a single AGN model does not provide a satisfactory fit to the data. This case can be most convincingly made for the nearest and most luminous SMBH binaries, where the single AGN model fit fails in the most obvious way: by having a poor χ^2 statistic. In the case of more distant ($z = 1$) or less luminous SMBH binaries (*LISA* sources) that are detected with a sufficient number of counts for a fit to be attempted, the case is more subtle. In such scenarios we find that the quality of the spectral fit may be adequate from a statistical (χ^2) standpoint but the value of the SMBH spin tends to be unconstrained. In addition to the anomalous spin measurements, in such cases the fits of the spectra with

Table 3. As in Table 2, but now assuming a *LISA* binary ($M = 10^6 M_\odot$). In this case, the composite SMBH binary spectrum is averaged over four phases of the orbit ($f = 0^\circ, 90^\circ, 180^\circ, \text{ and } 270^\circ$) since the 100 ks exposure time is comparable to the orbital period of the binary.

z	$\chi^2 / \text{d.o.f.}$	a	Γ	$\log \xi$	A_{Fe}	f_{ref}
<i>NewAthena</i> (X-IFU)						
0.1	76 / 89	$0.926^{+0.072p}_{-1.703}$	$2.09^{+0.08}_{-0.14}$	$1.31^{+0.65}_{-0.84}$	$8.89^{+1.11p}_{-8.39p}$	$4.11^{+3.17}_{-2.91}$
<i>NewAthena</i> (WFI)						
0.1	166 / 150	$0.498^{+0.500p}_{-1.496p}$	$2.00^{+0.10}_{-0.17}$	$2.30^{+1.70}_{-2.19}$	$0.50^{+9.50p}_{-0p}$	$0.46^{+1.79}_{-0.38}$
<i>AXIS</i>						
0.1	109 / 98	$-0.180^{+1.178p}_{-0.818p}$	$2.03^{+0.55}_{-0.94}$	$1.92^{+2.18}_{-1.92p}$	$0.50^{+9.50p}_{-0p}$	$2.54^{+7.46p}_{-2.43}$
<i>HEX-P</i>						
0.1	29 / 28	$-0.139^{+1.137p}_{-0.859p}$	$1.58^{+0.29}_{-0.24}$	$3.22^{+0.85}_{-1.34}$	$6.97^{+4.92}_{-3.03p}$	$9.70^{+0.30p}_{-8.86}$
<i>STROBE-X</i>						
0.1	150 / 154	$0.989^{+0.009p}_{-1.987p}$	$1.10^{+0.48}_{-0.10p}$	$3.54^{+1.16p}_{-0.47}$	$5.11^{+4.89p}_{-3.85}$	$10.00^{+0.00p}_{-10.00p}$

NOTE—At redshifts $z = 1.0$, although sources are detectable and their spectral shape potentially identifiable as characteristically AGN-like, the predicted count rates are insufficient for spectral analysis and χ^2 statistics with a 100 ks exposure.

Table 4. As in Table 2, but now fitting simulated *NewAthena* spectra of a $q = 0.2$ PTA binary at $z = 0.1$ observed at three different phases (Fig. 5). The goal of these fits is to search for orbital effects around the Fe K α line so all fits are performed between 2 and 12 keV. Due to the higher predicted count rates, the simulated spectra are re-grouped so that each bin contains at least 50 counts.

f	$\chi^2 / \text{d.o.f.}$	a	Γ	$\log \xi$	A_{Fe}	f_{ref}
<i>NewAthena</i> (X-IFU)						
90	5,828 / 5,920	$0.454^{+0.279}_{-1.452p}$	$1.95^{+0.01}_{-0.03}$	$3.01^{+0.28}_{-0.13}$	$0.53^{+0.08}_{-0.03p}$	$0.55^{+0.14}_{-0.10}$
180	5,886 / 5,933	$0.610^{+0.181}_{-0.434}$	1.96 ± 0.02	$3.00^{+0.07}_{-0.14}$	$0.57^{+0.15}_{-0.07p}$	$0.72^{+0.23}_{-0.14}$
270	5,886 / 5,933	$0.605^{+0.157}_{-0.225}$	2.11 ± 0.03	$1.38^{+0.25}_{-0.80}$	$0.87^{+0.11}_{-0.10}$	$1.49^{+0.27}_{-0.25}$
<i>NewAthena</i> (WFI)						
90	842 / 836	$-0.998^{+0.783}_{-0.000p}$	$1.91^{+0.01}_{-0.02}$	$3.28^{+0.07}_{-0.09}$	$0.51^{+0.08}_{-0.01p}$	$0.62^{+0.70}_{-0.13}$
180	842 / 834	$0.617^{+0.173}_{-0.172}$	$1.94^{+0.04}_{-0.02}$	$3.06^{+0.12}_{-0.22}$	$0.71^{+0.25}_{-0.13}$	$0.71^{+0.24}_{-0.15}$
270	777 / 833	$0.992^{+0.006p}_{-0.493}$	$1.95^{+0.01}_{-0.04}$	$3.08^{+0.14}_{-0.22}$	$0.61^{+0.05}_{-0.11}$	$1.29^{+0.18}_{-0.56}$

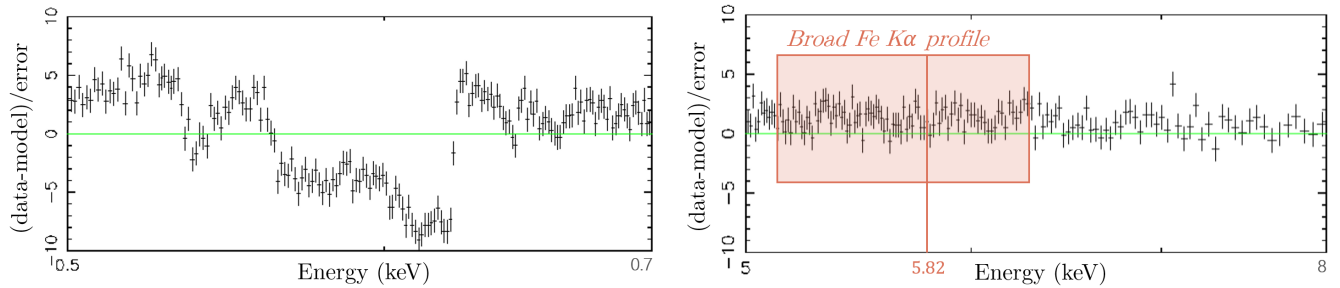


Figure 8. Left: The 0.5 to 0.7 keV residuals found after fitting the 100 ks mock X-IFU observation of a $z = 0.1$ PTA SMBH binary with a single AGN model (see Table 2). The high spectral resolution of the X-IFU reveals the complex combination of lines and emission features that are predicted in the composite SMBH binary model (Fig. 6). Right: As in the left panel, but now focused on the energy band that encompasses the Fe $K\alpha$ line (around 5.8 to 6.0 keV at $z=0.1$). The orange box highlights the extent of the broad Fe $K\alpha$ line profile; a line marks its rest energy, $6.4/(1+z) = 5.82$ keV at $z = 0.1$. While the X-IFU cannot resolve the small double-peak predicted by the composite spectrum, the clear excess flux between 5 and 6 keV, as evidenced by the consistently positive residuals, is consistent with the presence of a second Fe $K\alpha$ line in the spectrum.

sufficient high energy coverage also tend to indicate relatively hard X-ray spectra, and sometimes (but not consistently) a large or poorly constrained abundance and reflection fraction.

In most cases included in our analysis, the Fe $K\alpha$ lines in one-epoch spectra are fit reasonably well with a single AGN model and do not show significant fit residuals. Even so, they seem to contain useful information about the spin of one or both SMBHs that can potentially be recovered from fit. Specifically, we find that in the case of the nearby and luminous SMBH binaries with $q \approx 1$, the single AGN model returns the spin value representative of the input spin we assigned to the two SMBHs in our model. While the universality of this outcome remains to be fully explored for a wide range of binary configurations (and in particular those with different values of the primary and secondary spins), it is intriguing as it may provide a way to place constraints on the spin of one or both SMBHs. This is of particular importance for the PTA-detected binaries, as GW parameter estimation in these systems is not expected to place constraints on the SMBH spins and the X-ray reflection spectroscopy may provide a unique opportunity to do so.

The nearby luminous X-ray sources associated with PTA-like massive SMBH binaries have one more important advantage: the X-ray spectroscopy can be used to probe different phases of the binary orbit, providing the opportunity to investigate the time-variable binary signatures. In the example of a $q = 0.2$ binary the time-variability effect is most pronounced in the spin measurement. Although the input spin of neither SMBH changes from one point on the orbit to another, the phase-dependent variation in the shape of the Fe $K\alpha$ emission-line profile causes the single AGN model to return widely varying best fit values. This evidence, reinforced by a substantial variation in the ionization parameter and the reflection fraction would point to unusual and possibly unique physical conditions in the nuclear accretion flow of the emitting source. Note that as a consequence of the widely varying inferred spin value in the case of the $q = 0.2$ SMBH binary, the fit does not consistently recover the input spin we assigned to the SMBHs. This is in apparent contrast with the $q \approx 1$ case discussed in the previous paragraph and it motivates the development of a more rigorous parameter estimation method for SMBH binaries that is beyond the scope of this study.

5.2. Binary Identification Capabilities of Future X-ray Missions

Our analysis indicates that all X-ray observatories examined here are to some degree sensitive to the fact that the composite SMBH binary X-ray spectrum cannot be optimally fit by a model of a single AGN. In the next few paragraphs we discuss the most effective observational strategies for the X-ray detection and follow-up of SMBH binaries that are GW sources.

The combination of large collecting area (0.60 m² at 1 keV) and high spectral resolution (≤ 4 eV at 7 keV) makes the X-IFU instrument on *NewAthena* a powerful tool for identifying SMBH binaries (M. Cruise et al. 2025). This is demonstrated in Figure 8 which shows the fit residuals from a mock X-IFU observation of the PTA binary at $z = 0.1$ (see also Table 2). The left panel shows the detailed residuals in the 0.5 – 0.7 keV band that result when fitting this spectrum with the single AGN model. The mix of soft X-ray recombination lines from two mini-disks with a velocity offset yields a rich series of residuals in the high-resolution X-IFU spectrum. The prominent soft X-ray residuals can also be identified in the simulated *AXIS* observation in the right panel of Figure 7. While any ionized absorption present along the line-of-sight (not accounted for in our model) will undoubtedly complicate the analysis, the features predicted to be present in the soft X-ray part of the *NewAthena* X-IFU and *AXIS* spectra may be prominent enough to reveal a SMBH binary.

The right panel of Fig. 8 shows the residuals around the Fe $K\alpha$ line when the X-IFU spectrum is fit with the single AGN model. The assumed 100 ks exposure time is not sufficient for the high spectral resolution of the X-IFU to detect the double-peaked composite Fe $K\alpha$ line profile due to the binary (Fig. 6). However, the residuals clearly show a positive excess between 5 and 6 keV resulting from the sum of the two red-wings in the Fe $K\alpha$ lines from both mini-disks. This significant excess, in concert with the large soft X-ray residuals illustrated in the other panel, could be compelling evidence for the presence of a SMBH binary.

When it comes to the instruments with the most reliable high energy X-ray coverage, like *HEX-P* and *STROBE-X*, the fits to their spectra seem to more often return anomalous values of the photon index, iron abundance and/or reflection fraction. This is most likely due to the enhanced Compton hump of the composite. Thus, the spectra obtained by such observatories may lead to a faster recognition that one is dealing with an unusual source.

The poor χ^2 statistic, unconstrained spin and unusual values of other parameters discussed above would be

much more suggestive of the binary presence if a GW detection of an inspiraling SMBH binary was announced in the same part of the sky. In such cases, the X-ray spectroscopy could be carried out as a part of the EM follow-up of a GW source. The GW localization regions of PTA detected binaries are however expected to be relatively large (corresponding to $\sim 10\text{s} - 100\text{s deg}^2$ on the sky; P. Petrov et al. 2024), compared to the fields of view of the X-ray instruments considered in this work (which tend to be comparable to or less than 0.4 deg^2). It follows that the most efficient way to obtain the X-ray spectroscopy would be after a precise location of the EM counterpart was determined from the archival data or by another instrument like the Wide Field Monitor (WFM) on *STROBE-X*, for which the instantaneous field of view covers about 32% of the sky. As noted before, SMBH binaries with orbital separations of $100 r_g$ constitute *LISA* precursor sources and are only going to be detected by it later in the inspiral and at merger. The GW localization region of *LISA*-detected binaries is expected to reach $\sim 0.1\text{ deg}^2$ at merger (A. Mangiagli et al. 2020), at which point all X-ray instruments considered in this work may be able to enclose it within their field of view.

5.3. Current Model Limitations

5.3.1. Systematic Uncertainties in Single Black Hole Reflection Spectroscopy

Sections 3 and 4 showed that evidence of SMBH binaries may be found in the combined X-ray reflection spectra from the two mini-disks. However, the properties of the predicted reflection features are almost entirely dependent on the density structure of the disks and the details of how they are irradiated. Therefore, it is important to consider the implications of our model assumptions and how they could impact the observational prospects of identifying SMBH binaries through X-ray spectroscopy.

A key assumption in our model setup is the presence of a static lamppost corona in both mini-disks. While observationally, the corona is consistent with being compact (e.g., R. C. Reis & J. M. Miller 2013), the lamppost geometry is likely an idealization. A corona that covers some fraction of the inner accretion disk will potentially produce an ionization pattern on the disk different from the one predicted by a lamppost corona, altering the emitted reflection spectrum. If the disk is overionized by an extended corona, reflection features would be weaker and harder to detect in observations. A dynamic corona will also impact the predicted reflection features in the binary spectrum. For example, an outflowing corona (e.g., A. M. Beloborodov 1999; T. Dauser et al. 2013; C. J. Bambi et al. 2024), regardless of its

geometry, would reduce the flux incident on the inner disk, lowering its ionization state and potentially amplifying reflection features. However, depending on the viewing angle, the outflowing corona can also beam the power-law continuum into the line-of-sight, enhancing its observed brightness and increasing the difficulty of detecting the reflection features. Therefore, an outflowing corona may either improve or decrease the chances of observing strong reflection features from a SMBH binary.

A similar give-and-take can occur with the assumed density structure of the mini-disks. The `relxillpCp` model used here assumes a Shakura-Sunyaev density profile and though it is common in the standard thin-disk model to scale central density with the SMBH mass, we fix the central density to 10^{15} cm^{-3} for all SMBH mini-disks (Sect. 2.3). This assumption stems from a necessity, as `relxillpCp`'s pre-tabulated values of photoionization quantities allow for a limited range of densities between 10^{15} to 10^{20} cm^{-3} . It is worth noting that this value of the central density is appropriate for $\sim 10^6 M_\odot$ SMBHs, whereas central densities predicted by the standard thin-disk model for $\sim 10^9 M_\odot$ SMBHs can be up to a few orders of magnitude lower. This causes a minor inconsistency in our model setup, because our calculation of the peak ionization parameters utilizes the dependence of the gas density on the SMBH mass from R. Svensson & A. A. Zdziarski (1994), as laid out in D. R. Ballantyne (2017). As a result, the mini-disks around $\sim 10^9 M_\odot$ SMBHs are characterized by higher ionizing fluxes in our models (because $F_X \propto \xi n_H$). Disks that are more highly ionized tend to produce "smoother" reflection spectra with fewer features, which would make the binary signatures predicted by our model less obvious and their identification more difficult. In that sense, our model errs on the side of being more conservative. In addition to this, the X-ray reflection features in the calculated spectra are subject to poorly understood details of accretion disks and corona shared with single SMBH models. For example, winds and outflows can also sometimes complicate the analysis of an AGN reflection spectrum – though in principle, an X-IFU observation would have the potential to be able to distinguish between outflows, winds and actual disk reflection features. Still, continued progress in modeling the detailed radiative and gas dynamics is needed to better quantify the expected reflection signatures from single SMBHs and binaries.

Finally, Section 3 showed that the orbital blueshifting of the secondary SMBH can broaden the high-energy edge of the Fe $K\alpha$ profile, in some cases by 0.5 keV or more. However, such a shift is not unique to binary or-

bital motion and can in fact be seen in the spectra of single AGN. For example, a higher inclination angle enhances relativistic Doppler shifting from disk rotation, and in strongly ionized single SMBH spectra ($\log \xi \geq 2.8$), the Fe K α line is dominated by FeXXV emission at 6.7 keV (A. C. Fabian et al. 2000; T. R. Kallman et al. 2004). Thus, an apparent shift of the blue edge in a single-epoch spectrum is not, on its own, a definitive binary signature. However, if the shift is particularly pronounced (which can be expected from higher inclination angles) or periodic (as determined from the multi-epoch spectra), conventional single-SMBH explanations may be insufficient, making the binary hypothesis more compelling.

5.3.2. Treatment of Binary Effects

In addition to the uncertainties pertaining to single-SMBH spectral modeling, the presence of a secondary source introduces further complexities, particularly through the addition of binary dynamics, geometric and relativistic effects. To make the problem tractable, we adopted simplifying assumptions regarding binary-specific parameters and considered only a subset of the full parameter space. Below, we discuss these choices in the context of our modeling approach.

We assume that the two mini-disks are co-planar with the binary orbital axis. This assumption is appropriate in scenarios where the angular momentum of the gas in the circumbinary disk is well defined and the binary orbit has had sufficient time to align with it through gravitational torques (e.g. T. Bogdanović et al. 2007; M. C. Miller & J. H. Krolik 2013). This specific geometry minimizes the effects of cross-illumination, where emission from one corona could in principle be reprocessed by the other mini-disk. We neglect this effect in our model, as it is most pronounced when the minidisks are misaligned with respect to each other. For misaligned minidisks, the incidence angle of ionizing radiation from the companion SMBH is larger, which may introduce non-axisymmetric ionization patterns in the mini-disks and potentially, the circumbinary disk (K. Nguyen & T. Bogdanović 2016). As a result, the X-ray spectra in those cases may be more readily distinguishable from those of AGN powered by a single SMBH (as shown by K. Nguyen et al. 2019, 2020, for optical spectra).

We also assume that the accretion rate through the two mini-disks is steady in time. Numerical simulations have found that for $q \gtrsim 0.1$, SMBH binaries can have enhanced periodicity in accretion rates onto the mini-disks on approximately the orbital time scale of the binary (e.g., B. D. Farris et al. 2015). Whether the time-dependent accretion rate through the accretion

streams onto the outer mini-disks propagates through to the accretion rate onto the black holes at the ISCO or is buffered by the mini-disks will depend on the spatial extent and properties of the mini-disks. To evaluate which scenario applies to the mini-disks considered in this work, we estimate the viscous time scale of the smallest mini-disk in the model and compare it to the binary orbital time. According to equation 3 and the estimates thereafter, the most compact mini-disk with $r_{\text{out}} \approx 13 r_g$ arises around the secondary SMBH in $q = 0.1$ binary. The viscous time scale of this disk can be estimated as $t_{\text{visc}} = -r_{\text{out}}/\dot{r}_{\text{visc}} \approx 16.4$ days, for the total mass of the binary $10^6 M_\odot$ and accretion rate on the secondary of $\lambda_2 = 0.5$. Here $\dot{r}_{\text{visc}} = -1.5\alpha (h/r)^2 v_{\text{Kep}}$ is the viscous inflow rate at the radius r_{out} of the mini-disk, $\alpha = 0.1$ is the dimensionless viscosity parameter, v_{Kep} is the circular speed of the gas in the disk, h/r is the geometric aspect ratio of the standard, radiation-pressure supported thin-disk (N. I. Shakura & R. A. Sunyaev 1973). Since $t_{\text{visc}} \gg t_{\text{orb}}$ (see equation 1) for this and all other considered configurations, we conclude that we are in the regime where the accretion rate variability though the streams will be buffered by the mini-disks, due to their long viscous time scales. The assumption of steady accretion rates onto the SMBHs therefore appears to be reasonable.

We have limited our analysis to scenarios where both SMBHs are expected to be accreting through a standard geometrically-thin, optically-thick disk. However, a non-negligible portion of the parameter space shown in Fig. 1 is occupied by configurations with either a super-Eddington secondary mini-disk or an extremely sub-Eddington primary mini-disk, regimes where the thin-disk picture is invalid. The X-ray spectral properties of these configurations also merit investigation but are outside of the scope of this work.

The shape of the Fe K α lines and the other reflection features predicted by the `relxillpCp` model depends not only on the ionization properties of the mini-disks, but also the spins of both SMBHs in the binary. We have assumed near-maximal spins ($a = 0.99$) for each SMBH, consistent with observations of bright AGNs (e.g., C. S. Reynolds 2021). High spins enhance the effects of relativistic blurring, and by decreasing the radius of closest stable orbit, allow emission from the deepest parts of the potential well, which is most strongly redshifted. However, there is some tentative evidence indicating that a may be systematically lower ($a \sim 0.7$) for SMBHs with masses $\gtrsim 10^8 M_\odot$, which would be applicable to PTA binaries. A lower SMBH spin will increase the ISCO and reduce the amount of gravitational redshift and relativistic blurring affecting the reflection spectra produced by

the mini-disks. If one or both of the SMBHs in a binary has a lower spin, then this could make the reflection features more prominent, improving the likelihood of finding evidence for the binary in the composite spectrum. We defer the exploration of a wider range of SMBH spin values to future work.

A small error is introduced in the computation of the special relativistic Doppler shift, due to the approximate way velocities are combined. In our calculation, the Doppler shift of each gas parcel in the mini-disks producing the reflection spectrum is divided into two separate components: (1) one due to the motion of the gas in the mini-disks relative to each BH’s rest-frame, computed by `relxill`, and (2) due to the binary orbital motion, which we compute separately. By computing these Doppler shifts sequentially, we are effectively adding the bulk velocity of the mini-disks to the Keplerian motion of the gas within them in a Galilean fashion. This introduces an error of the order of a few percent to our calculation. For example, consider an emitting fluid element located in a mini-disk at a radius of $18 r_g$ from its MBH. For a $q = 1$ binary at an orbital separation of $100 r_g$ (where the orbital velocity of the binary is $0.1c$), the maximum difference in the proper velocity of the fluid between a Galilean velocity transformation and the correct special relativistic treatment through Lorentz transformations is about 1.7%. This level of error remains within acceptable limits for the purposes of our analysis.

6. CONCLUSIONS

X-ray reflection signatures are important features in the spectra of AGNs, providing general information on the physics of accretion disks, as well as probing the space-time geometry around the central SMBH. It is therefore reasonable to expect that the reflection signal from the two SMBHs in a binary will show evidence of the presence of the binary, and could even allow measurements of the spins of SMBHs. In this paper, we developed a model to predict the reflection spectra of SMBH binaries at an orbital separation of $100 r_g$ with different mass ratios and Eddington accretion rates. Limiting ourselves to the regime of geometrically-thin, optically-thick mini-disks, we calculated the relativistic ionized reflection spectra from both mini-disks and produced a combined X-ray spectrum from the binary. Our main findings are as follows:

- The reflection features are strongly influenced by the accretion-inversion phenomenon expected in SMBH binaries, which results in a wide range of ionization conditions in the mini-disks and the resulting composite reflection spectrum. The impact

of the binary is not uniform across the composite spectrum – in some scenarios, only the high energy reflection hump is enhanced, while in others, the impact is isolated to a mixture of soft X-ray emission lines. The SMBH binary configurations investigated here also give rise to the variable double-peaked relativistic Fe $K\alpha$ line profiles and a shift of the blue edge of the line amounting to about 0.5 keV associated with their orbital motion (Section 3).

- To understand whether these features are distinct enough to be used as smoking guns for the presence of SMBH binaries, we calculated mock 100 ks observations of one of the configurations with *NewAthena*, *AXIS*, *HEX-P*, and *STROBE-X* and fit them with a single AGN model (Section 4). We find that, in the absence of very high-count rate data when the fit fails obviously, with a poor χ^2 statistic, evidence for a binary may also be found from unusual parameter values when fitting a single-epoch spectrum.
- For a nearby PTA binary ($10^9 M_\odot$ at $z = 0.1$) the single AGN model most obviously failed to fit the data, with strong residuals between 0.5 and 0.7 keV and weak residuals around the Fe $K\alpha$ line. If this binary is instead at $z = 1$, the decreased count rate masks most signs of binarity and the single AGN model becomes an acceptable fit to the mock data – even with the large collecting area of *NewAthena*. The fits at $z = 1$ were however all unable to constrain an SMBH spin in the mock data, indicating that the altered shape of the Fe $K\alpha$ line is preventing the fitting model from converging to a single value.
- For fainter SMBH binaries that are progenitors of *LISA* sources ($10^6 M_\odot$), spectral fitting with 100-ks observations is only possible for a source at $z = 0.1$. The single AGN model also provides a good fit to the single-epoch mock spectrum in this case but with similar challenges in constraining the SMBH spin as for the PTA binaries with $z = 1$.
- In binaries with orbital time longer than 100 ks observations, multi-epoch exposures can capture spectral variability caused by the binary orbital motion. The shape of the Fe $K\alpha$ line is predicted to change in this sequence of spectra, and, indeed, we find that high count-rate *NewAthena* spectra of a PTA binary at $z = 0.1$ show significant epoch-to-epoch changes in the SMBH spin when fit with a single AGN model. Such a result, combined with

soft X-ray residuals that also vary with each exposure, could be compelling evidence for the presence of a SMBH binary. In the case of the *LISA* binary configurations considered here, 100 ks exposure is longer than the orbital time, resulting in the averaging and loss of spectral variability signatures associated with their orbital motion.

Reflection spectra from accretion disks are sensitive to the assumed density structure of the disk and details of how they are illuminated by the X-ray emitting corona. In addition, there remain uncertainties in the properties of mini-disks around the two SMBHs, their relative geometries, and their interaction with the surrounding CBD. The results presented here should be considered an initial proof-of-concept study that will be expanded upon in future work. Nevertheless, it is clear that reflection signatures in the X-ray spectra of SMBH bina-

ries will contain evidence for the presence of the binary. Deep X-ray observations of such sources may be able to unravel the components from both mini-disks, allowing insight into the evolution of SMBH binaries prior to merger.

ACKNOWLEDGEMENTS

J.M., T.B., D.R.B., T.D. acknowledge support from the NSF grant AST-2307278 and L.B. from the NSF grant AST-2307279. D.R.B. is also supported from NASA award 80NSSC24K0212 and NSF grant AST-2407658. T.D. acknowledges support from the DFG research unit FOR 5195 (project number 443220636, grant number WI 1860/20-1).

REFERENCES

- Agazie, G., Anumalapudi, A., Archibald, A. M., et al. 2023a, *ApJL*, 951, L8, doi: [10.3847/2041-8213/acdac6](https://doi.org/10.3847/2041-8213/acdac6)
- Agazie, G., Anumalapudi, A., Archibald, A. M., et al. 2023b, *ApJL*, 951, L50, doi: [10.3847/2041-8213/ace18a](https://doi.org/10.3847/2041-8213/ace18a)
- Antoniadis, J., Arumugam, P., Arumugam, S., et al. 2023, *A&A*, 678, A50, doi: [10.1051/0004-6361/202346844](https://doi.org/10.1051/0004-6361/202346844)
- Antonini, F., Barausse, E., & Silk, J. 2015, *ApJ*, 812, 72, doi: [10.1088/0004-637X/812/1/72](https://doi.org/10.1088/0004-637X/812/1/72)
- Arnaud, K. A. 1996, in *Astronomical Society of the Pacific Conference Series*, Vol. 101, *Astronomical Data Analysis Software and Systems V*, ed. G. H. Jacoby & J. Barnes, 17
- Artymowicz, P., & Lubow, S. H. 1994, *ApJ*, 421, 651, doi: [10.1086/173679](https://doi.org/10.1086/173679)
- Avara, M. J., Krolik, J. H., Campanelli, M., et al. 2024, *ApJ*, 974, 242, doi: [10.3847/1538-4357/ad5bda](https://doi.org/10.3847/1538-4357/ad5bda)
- Ballantyne, D. R. 2017, *MNRAS*, 472, L60, doi: [10.1093/mnras/slx138](https://doi.org/10.1093/mnras/slx138)
- Ballantyne, D. R. 2020, *MNRAS*, 491, 3553, doi: [10.1093/mnras/stz3294](https://doi.org/10.1093/mnras/stz3294)
- Bambic, C. J., Quataert, E., & Kunz, M. W. 2024, *MNRAS*, 527, 2895, doi: [10.1093/mnras/stad3261](https://doi.org/10.1093/mnras/stad3261)
- Barnes, J. E., & Hernquist, L. E. 1991, *ApJ*, 370, L65, doi: [10.1086/185978](https://doi.org/10.1086/185978)
- Begelman, M. C., Blandford, R. D., & Rees, M. J. 1980, *Nature*, 287, 307, doi: [10.1038/287307a0](https://doi.org/10.1038/287307a0)
- Beloborodov, A. M. 1999, *ApJL*, 510, L123, doi: [10.1086/311810](https://doi.org/10.1086/311810)
- Blaes, O. 2014, *SSRv*, 183, 21, doi: [10.1007/s11214-013-9985-6](https://doi.org/10.1007/s11214-013-9985-6)
- Blandford, R. D., & Znajek, R. L. 1977, *MNRAS*, 179, 433, doi: [10.1093/mnras/179.3.433](https://doi.org/10.1093/mnras/179.3.433)
- Bogdanović, T., Eracleous, M., & Sigurdsson, S. 2009, *NewAR*, 53, 113, doi: [10.1016/j.newar.2009.09.005](https://doi.org/10.1016/j.newar.2009.09.005)
- Bogdanović, T., Miller, M. C., & Blecha, L. 2022, *Living Reviews in Relativity*, 25, 3, doi: [10.1007/s41114-022-00037-8](https://doi.org/10.1007/s41114-022-00037-8)
- Bogdanović, T., Reynolds, C. S., & Miller, M. C. 2007, *ApJ*, 661, L147, doi: [10.1086/518769](https://doi.org/10.1086/518769)
- Bowen, D. B., Campanelli, M., Krolik, J. H., Mewes, V., & Noble, S. C. 2017, *ApJ*, 838, 42, doi: [10.3847/1538-4357/aa63f3](https://doi.org/10.3847/1538-4357/aa63f3)
- Brenneman, L. W., & Reynolds, C. S. 2006, *ApJ*, 652, 1028, doi: [10.1086/508146](https://doi.org/10.1086/508146)
- Cruise, M., Guainazzi, M., Aird, J., et al. 2025, *arXiv e-prints*, arXiv:2501.03100, doi: [10.48550/arXiv.2501.03100](https://doi.org/10.48550/arXiv.2501.03100)
- d’Ascoli, S., Noble, S. C., Bowen, D. B., et al. 2018, *ApJ*, 865, 140, doi: [10.3847/1538-4357/aad8b4](https://doi.org/10.3847/1538-4357/aad8b4)
- Dauser, T., Garcia, J., Parker, M. L., Fabian, A. C., & Wilms, J. 2014, *MNRAS*, 444, L100, doi: [10.1093/mnras/slu125](https://doi.org/10.1093/mnras/slu125)
- Dauser, T., García, J., Walton, D. J., et al. 2016, *A&A*, 590, A76, doi: [10.1051/0004-6361/201628135](https://doi.org/10.1051/0004-6361/201628135)
- Dauser, T., Garcia, J., Wilms, J., et al. 2013, *MNRAS*, 430, 1694, doi: [10.1093/mnras/sts710](https://doi.org/10.1093/mnras/sts710)
- Dauser, T., García, J. A., Joyce, A., et al. 2022, *MNRAS*, 514, 3965, doi: [10.1093/mnras/stac1593](https://doi.org/10.1093/mnras/stac1593)
- Davis, S. W., & Laor, A. 2011, *ApJ*, 728, 98, doi: [10.1088/0004-637X/728/2/98](https://doi.org/10.1088/0004-637X/728/2/98)

- De Rosa, A., Vignali, C., Bogdanović, T., et al. 2019, *NewAR*, 86, 101525, doi: [10.1016/j.newar.2020.101525](https://doi.org/10.1016/j.newar.2020.101525)
- Di Matteo, T., Springel, V., & Hernquist, L. 2005, *Nature*, 433, 604, doi: [10.1038/nature03335](https://doi.org/10.1038/nature03335)
- Duras, F., Bongiorno, A., Ricci, F., et al. 2020, *A&A*, 636, A73, doi: [10.1051/0004-6361/201936817](https://doi.org/10.1051/0004-6361/201936817)
- Eggleton, P. P. 1983, *ApJ*, 268, 368, doi: [10.1086/160960](https://doi.org/10.1086/160960)
- Eracleous, M., Boroson, T. A., Halpern, J. P., & Liu, J. 2012, *ApJS*, 201, 23, doi: [10.1088/0067-0049/201/2/23](https://doi.org/10.1088/0067-0049/201/2/23)
- Fabian, A. C., Iwasawa, K., Reynolds, C. S., & Young, A. J. 2000, *Publications of the Astronomical Society of the Pacific*, 112, 1145, doi: [10.1086/316610](https://doi.org/10.1086/316610)
- Fabian, A. C., Lohfink, A., Kara, E., et al. 2015, *MNRAS*, 451, 4375, doi: [10.1093/mnras/stv1218](https://doi.org/10.1093/mnras/stv1218)
- Fabian, A. C., Rees, M. J., Stella, L., & White, N. E. 1989, *MNRAS*, 238, 729, doi: [10.1093/mnras/238.3.729](https://doi.org/10.1093/mnras/238.3.729)
- Farris, B. D., Duffell, P., MacFadyen, A. I., & Haiman, Z. 2014, *ApJ*, 783, 134, doi: [10.1088/0004-637X/783/2/134](https://doi.org/10.1088/0004-637X/783/2/134)
- Farris, B. D., Duffell, P., MacFadyen, A. I., & Haiman, Z. 2015, *MNRAS*, 446, L36, doi: [10.1093/mnrasl/slu160](https://doi.org/10.1093/mnrasl/slu160)
- Foord, A., Cappelluti, N., Liu, T., et al. 2024, *Universe*, 10, 237, doi: [10.3390/universe10060237](https://doi.org/10.3390/universe10060237)
- Fukumura, K., & Kazanas, D. 2007, *ApJ*, 664, 14, doi: [10.1086/518883](https://doi.org/10.1086/518883)
- García, J., & Kallman, T. R. 2010, *ApJ*, 718, 695, doi: [10.1088/0004-637X/718/2/695](https://doi.org/10.1088/0004-637X/718/2/695)
- Günther, R., & Kley, W. 2002, *A&A*, 387, 550, doi: [10.1051/0004-6361:20020407](https://doi.org/10.1051/0004-6361:20020407)
- Hayasaki, K., Mineshige, S., & Sudou, H. 2007, *PASJ*, 59, 427, doi: [10.1093/pasj/59.2.427](https://doi.org/10.1093/pasj/59.2.427)
- Hopkins, P. F., Hernquist, L., Cox, T. J., et al. 2005, *ApJ*, 630, 705, doi: [10.1086/432438](https://doi.org/10.1086/432438)
- Hopkins, P. F., Hernquist, L., Cox, T. J., & Kereš, D. 2008, *ApJS*, 175, 356, doi: [10.1086/524362](https://doi.org/10.1086/524362)
- Husemann, B., Heidt, J., De Rosa, A., et al. 2020, *A&A*, 639, A117, doi: [10.1051/0004-6361/202037988](https://doi.org/10.1051/0004-6361/202037988)
- Jovanović, P., Borka Jovanović, V., Borka, D., & Bogdanović, T. 2014, *Advances in Space Research*, 54, 1448, doi: [10.1016/j.asr.2013.10.028](https://doi.org/10.1016/j.asr.2013.10.028)
- Jovanović, P., Borka Jovanović, V., Borka, D., & Popović, L. Č. 2020, *Contributions of the Astronomical Observatory Skalnaté Pleso*, 50, 219, doi: [10.31577/caosp.2020.50.1.219](https://doi.org/10.31577/caosp.2020.50.1.219)
- Kallman, T. R., Palmeri, P., Bautista, M. A., Mendoza, C., & Krolik, J. H. 2004, *The Astrophysical Journal Supplement Series*, 155, 675, doi: [10.1086/424039](https://doi.org/10.1086/424039)
- Kazantzidis, S., Mayer, L., Colpi, M., et al. 2005, *The Astrophysical Journal*, 623, L67, doi: [10.1086/430139](https://doi.org/10.1086/430139)
- Keek, L., & Ballantyne, D. R. 2016, *MNRAS*, 456, 2722, doi: [10.1093/mnras/stv2882](https://doi.org/10.1093/mnras/stv2882)
- Kelley, L. Z., Haiman, Z., Sesana, A., & Hernquist, L. 2019, *MNRAS*, 485, 1579, doi: [10.1093/mnras/stz150](https://doi.org/10.1093/mnras/stz150)
- Lin, D. N. C., & Papaloizou, J. 1979, *MNRAS*, 186, 799, doi: [10.1093/mnras/186.4.799](https://doi.org/10.1093/mnras/186.4.799)
- MacFadyen, A. I., & Milosavljević, M. 2008, *ApJ*, 672, 83, doi: [10.1086/523869](https://doi.org/10.1086/523869)
- Madsen, K. K., García, J. A., Stern, D., et al. 2024, *Frontiers in Astronomy and Space Sciences*, 11, 1357834, doi: [10.3389/fspas.2024.1357834](https://doi.org/10.3389/fspas.2024.1357834)
- Mangiagli, A., Caprini, C., Volonteri, M., et al. 2022, *PhRvD*, 106, 103017, doi: [10.1103/PhysRevD.106.103017](https://doi.org/10.1103/PhysRevD.106.103017)
- Mangiagli, A., Klein, A., Bonetti, M., et al. 2020, *PhRvD*, 102, 084056, doi: [10.1103/PhysRevD.102.084056](https://doi.org/10.1103/PhysRevD.102.084056)
- Martocchia, A., & Matt, G. 1996, *MNRAS*, 282, L53, doi: [10.1093/mnras/282.4.L53](https://doi.org/10.1093/mnras/282.4.L53)
- Meidinger, N., Albrecht, S., Beitle, C., et al. 2020, in *Society of Photo-Optical Instrumentation Engineers (SPIE) Conference Series*, Vol. 11444, *Space Telescopes and Instrumentation 2020: Ultraviolet to Gamma Ray*, ed. J.-W. A. den Herder, S. Nikzad, & K. Nakazawa, 114440T, doi: [10.1117/12.2560507](https://doi.org/10.1117/12.2560507)
- Miller, M. C., & Krolik, J. H. 2013, *ApJ*, 774, 43, doi: [10.1088/0004-637x/774/1/43](https://doi.org/10.1088/0004-637x/774/1/43)
- Nguyen, K., & Bogdanović, T. 2016, *ApJ*, 828, 68, doi: [10.3847/0004-637X/828/2/68](https://doi.org/10.3847/0004-637X/828/2/68)
- Nguyen, K., Bogdanović, T., Runnoe, J. C., et al. 2019, *ApJ*, 870, 16, doi: [10.3847/1538-4357/aaeff0](https://doi.org/10.3847/1538-4357/aaeff0)
- Nguyen, K., Bogdanović, T., Runnoe, J. C., et al. 2020, *ApJ*, 894, 105, doi: [10.3847/1538-4357/ab88b5](https://doi.org/10.3847/1538-4357/ab88b5)
- Paczynski, B., & Rudak, B. 1980, *AcA*, 30, 237
- Papaloizou, J., & Pringle, J. E. 1977, *MNRAS*, 181, 441, doi: [10.1093/mnras/181.3.441](https://doi.org/10.1093/mnras/181.3.441)
- Peters, P. C. 1964, *Physical Review*, 136, B1224, doi: [10.1103/physrev.136.b1224](https://doi.org/10.1103/physrev.136.b1224)
- Peters, P. C., & Mathews, J. 1963, *Physical Review*, 131, 435, doi: [10.1103/PhysRev.131.435](https://doi.org/10.1103/PhysRev.131.435)
- Petrov, P., Taylor, S. R., Charisi, M., & Ma, C.-P. 2024, *ApJ*, 976, 129, doi: [10.3847/1538-4357/ad7b1410.1134/S1063772908070032](https://doi.org/10.3847/1538-4357/ad7b1410.1134/S1063772908070032)
- Pichardo, B., Sparke, L. S., & Aguilar, L. A. 2005, *MNRAS*, 359, 521, doi: [10.1111/j.1365-2966.2005.08905.x](https://doi.org/10.1111/j.1365-2966.2005.08905.x)
- Popović, L. Č. 2012, *NewAR*, 56, 74, doi: [10.1016/j.newar.2011.11.001](https://doi.org/10.1016/j.newar.2011.11.001)
- Ramos Almeida, C., & Ricci, C. 2017, *Nature Astronomy*, 1, 679, doi: [10.1038/s41550-017-0232-z](https://doi.org/10.1038/s41550-017-0232-z)
- Ray, P. S., Roming, P. W. A., Argan, A., et al. 2024, *arXiv e-prints*, arXiv:2410.08342, doi: [10.48550/arXiv.2410.08342](https://doi.org/10.48550/arXiv.2410.08342)
- Reardon, D. J., Zic, A., Shannon, R. M., et al. 2023, *ApJL*, 951, L6, doi: [10.3847/2041-8213/acdd02](https://doi.org/10.3847/2041-8213/acdd02)

- Reis, R. C., & Miller, J. M. 2013, *ApJL*, 769, L7, doi: [10.1088/2041-8205/769/1/L7](https://doi.org/10.1088/2041-8205/769/1/L7)
- Reynolds, C., Kara, E., Mushotzky, R. F., et al. 2023, in *UV, X-Ray, and Gamma-Ray Space Instrumentation for Astronomy XXIII*, ed. O. H. Siegmund & K. Hoadley (SPIE), 49, doi: [10.1117/12.2677468](https://doi.org/10.1117/12.2677468)
- Reynolds, C. S. 2013, *Classical and Quantum Gravity*, 30, 244004, doi: [10.1088/0264-9381/30/24/244004](https://doi.org/10.1088/0264-9381/30/24/244004)
- Reynolds, C. S. 2021, *ARA&A*, 59, doi: [10.1146/annurev-astro-112420-035022](https://doi.org/10.1146/annurev-astro-112420-035022)
- Reynolds, C. S., & Fabian, A. C. 2008, *ApJ*, 675, 1048, doi: [10.1086/527344](https://doi.org/10.1086/527344)
- Roedig, C., Dotti, M., Sesana, A., Cuadra, J., & Colpi, M. 2011, *MNRAS*, 415, 3033, doi: [10.1111/j.1365-2966.2011.18927.x](https://doi.org/10.1111/j.1365-2966.2011.18927.x)
- Roedig, C., Krolik, J. H., & Miller, M. C. 2014, *ApJ*, 785, 115, doi: [10.1088/0004-637X/785/2/115](https://doi.org/10.1088/0004-637X/785/2/115)
- Ross, R. R., & Fabian, A. C. 2005, *MNRAS*, 358, 211, doi: [10.1111/j.1365-2966.2005.08797.x](https://doi.org/10.1111/j.1365-2966.2005.08797.x)
- Runnoe, J. C., Cales, S., Ruan, J. J., et al. 2015, *MNRAS*, 455, 1691, doi: [10.1093/mnras/stv2385](https://doi.org/10.1093/mnras/stv2385)
- Sesana, A., Roedig, C., Reynolds, M. T., & Dotti, M. 2012, *MNRAS*, 420, 860, doi: [10.1111/j.1365-2966.2011.20097.x](https://doi.org/10.1111/j.1365-2966.2011.20097.x)
- Shakura, N. I., & Sunyaev, R. A. 1973, *A&A*, 24, 337
- Svensson, R., & Zdziarski, A. A. 1994, *ApJ*, 436, 599, doi: [10.1086/174934](https://doi.org/10.1086/174934)
- Tanaka, Y., Nandra, K., Fabian, A. C., et al. 1995, *Nature*, 375, 659, doi: [10.1038/375659a0](https://doi.org/10.1038/375659a0)
- Tang, Y., Haiman, Z., & MacFadyen, A. 2018, *MNRAS*, 476, 2249, doi: [10.1093/mnras/sty423](https://doi.org/10.1093/mnras/sty423)
- Volonteri, M., Haardt, F., & Madau, P. 2003, *ApJ*, 582, 559, doi: [10.1086/344675](https://doi.org/10.1086/344675)
- Xu, H., Chen, S., Guo, Y., et al. 2023, *Research in Astronomy and Astrophysics*, 23, 075024, doi: [10.1088/1674-4527/acdfa5](https://doi.org/10.1088/1674-4527/acdfa5)
- Yu, Q., & Lu, Y. 2001, *A&A*, 377, 17, doi: [10.1051/0004-6361:20011064](https://doi.org/10.1051/0004-6361:20011064)

APPENDIX

A. INSTRUMENT SIMULATION FILES AND CHARACTERISTICS

Table A1. Response, ancillary and background files used to simulate 100 ks observations of the SMBH binary model (e.g., Fig. 6). All simulations are generated using the `fakeit` command in `Xspec`.

Instrument	Response files
<i>NewAthena</i>	
WFI	athena_wfi_rmf_v20230523.rmf NewAthena_WFI_13rows_FD_w_filter_OnAxis_20240209.arf NewAthena_WFI_13rows_FD_20240223_bkgd_sum_1amin_w_filter_OnAxis.pha
X-IFU	athena_xifu_3eV_gaussian.rmf athena_xifu_13_rows_thick_optical_filter.arf athena_xifu_nxb_1pix.pha
<i>AXIS</i>	
XMA	axis_ccd_20221101.rmf axis_onaxis_20230701.arf axis_nxb_FOV_10Msec_20221215.pha
<i>HEX-P</i>	
LET	HEXP_LET_v09.rmf HEXP_LET_v09_PSFcor.arf HEXP_LET_v09_L1_R8arcsec.bkg
HET	HEXP_HET_v09.rmf HEXP_HET_v09_PSFcor_x2.arf HEXP_HET_v09_x2_L1_R18arcsec_Ln25keV.bkg
<i>STROBE-X</i>	
LEMA	lema_2017-08-11.rmf lema_60_2023-11-16.arf lema_nxb_plus_cxb.bkg
HEMA300	STROBEX_HEMA_300eV.rmf STROBEX_HEMA_300eV.arf STROBEX_HEMA_300eV.bkg

Table A2. Nominal bandpass, collecting area and energy resolution of each proposed instrument included in this study.

Mission	Instrument	Nominal bandpass	Collecting area at 6 keV	Energy resolution
<i>NewAthena</i>	WFI	0.1-15 keV	1,780 cm ²	80 eV (at 1 keV), <170 eV (at 7 keV)
	X-IFU	0.2-12 keV	1,220 cm ²	4 eV (at 7 keV)
<i>AXIS</i>	XMA	0.3-10 keV	830 cm ²	70 eV (at 1 keV), 150 eV (at 6 keV)
<i>HEX-P</i>	LET	0.2-20 keV	530 cm ²	80 eV (at 1 keV), 150 eV (at 7 keV)
	HET	2-80 keV	140 cm ²	500 eV (below 10 keV), 850 eV (at 60 keV)
<i>STROBE-X</i>	LEMA	0.2-12 keV	2,980 cm ²	85 eV (at 1 keV)
	HEMA300	2-30 keV	32,990 cm ²	300-500 eV (at 6.4 keV)

NOTE—Numbers for the collecting area are sourced directly from the `.arf` files for each instrument. References for the nominal bandpass and energy resolution are taken from the following sources: [N. Meidinger et al. \(2020\)](#) and [M. Cruise et al. \(2025\)](#) for *NewAthena*, [C. Reynolds et al. \(2023\)](#) for *AXIS*, [K. K. Madsen et al. \(2024\)](#) for *HEX-P* and [P. S. Ray et al. \(2024\)](#) for *STROBE-X*.